The University of Sydney

Department of Civil Engineering
Sydney NSW 2006
AUSTRALIA

http://www.civil.usyd.edu.au/

Environmental Fluids/Wind Group

Spring-neap tide-induced beach water table fluctuations and its influence on the behaviour of a coastal aquifer adjacent to a low-relief estuary

Research Report No R856

D-S Jeng, BE ME PhD
X. Mao, BE ME PhD
P. Enot, BE ME PhD
D. A. Barry, BSc PhD
L. Li, BE MPhil PhD
A. Binlet, BE PhD

November 2005

The University of Sydney

Department of Civil Engineering
Environmental Fluids/Wind Group
http://www.civil.usyd.edu.au/

Spring-neap tide-induced beach water table fluctuations and its influence on the behaviour of a coastal aquifer adjacent to a low-relief estuary

Research Report No R856

D-S Jeng, BE ME PhD
X. Mao, BE ME PhD
P. Enot, BE ME PhD
D. A. Barry, BSc PhD
L. Li, BE MPhil PhD
A. Binlet, BE PhD

November 2005

Abstract:

In this study, we investigated the effect of beach slope for a coastal aquifer adja-cent to a low-relief estuary. The waste was suspected to discharge leachate towards the estuary. Field observations at various locations showed that tidally induced groundwater head fluctuations were skewed temporally. Frequency analysis suggested that the fluctuation amplitudes de-creased exponentially and the phase-lags increased linearly for the primary tidal signals as they propagated inland. Flow and transport processes in a cross-section perpendicular to the estuary were simulated using SEAWAT-2000, which is capable of depicting density-dependent flow and multi-species transport. The simulations showed that the modelled water table fluctuations were in good agreement with the monitored data. The simulations showed that density difference and tidal forcing drive a more complex hydrodynamic pattern for the mildly sloping beach than the vertical beach, as well as a profound asymmetry in tidally induced water table fluctuations and enhanced salt-water intrusion. The simulation results also indicated that contaminant transport from the aquifer to the estuary was affected by the tide.

Keywords:

SEAWAT-2000; Salt-water intrusion; Water table fluctuation; Numerical model; Submarine groundwater discharge

Copyright Notice

Department of Civil Engineering, Research Report R856
Spring-neap tide-induced beach water table fluctuations and its influence on the behaviour of a coastal aquifer adjacent to a low-relief estuary

d.jeng@civil.usyd.edu.au,

Published by:
Department of Civil Engineering
The University of Sydney
Sydney NSW 2006
AUSTRALIA

November 2005

This report and other Research Reports published by The Department of Civil Engineering are available on the Internet:

http://www.civil.usyd.edu.au

Contents

1. Introduction

Serious environmental problems often occur in coastal areas that are densely populated or have been industrialised. Challenges include salt-water intrusion due to groundwater pumping and brine discharges from desalination plants, as well as coastal (estuarine) water pollution by plume leachate from contaminated coastal aquifers (e.g., Bear et al., 1999; Purnalna, et al., 2003; Ullman et al., 2003).

Coastal aquifers are complex zones due to the combined influences of oceanic oscillations and inland groundwater forcing. These influences lead to complex behaviour of subsurface contaminants discharging into the sea/estuary. Important, unique factors of a coastal aquifer system include the influence of the density contrast between the salt water and fresh groundwater, tidal fluctuations and the effect of beach slope. Their net effects lead to complicated hydrodynamic conditions in coastal aquifers, which in turn could influence the local ecological environment (Ataie-Ashtiani et al., 1999a; Bear et al., 1999).

Three topics related to the behaviour of coastal aquifers have been intensively investigated in the past few decades: tide-induced groundwater fluctuations, salt-water intrusion and contaminant transport/submarine groundwater discharge (SGD) from the coastal aquifer to the adjacent estuary/coastal sea. We discuss each topic briefly below.

Analytical solutions have been vigorously pursued in modelling of tide-induced groundwater fluctuations, with solutions available for quantifying the effect of the vertical beach, sloping beach, aquifer leakage, density differences and varying tidal signal along the estuary (e.g., Nielsen, 1990; Barry et al., 1996; Jiao and Tang, 1999; Li et al., 1997, 2000a-d; Cheng and Ouazar, 2003; Su et al., 2003; Teo et al., 2003, Jeng et al., 2005a). These solutions show that when the tidal signal propagates inland, the amplitude of the groundwater fluctuation decreases exponentially while the phase of the signal is shifted. As most analytical solutions are based on the assumption of a homogeneous aquifer, uniform beach slope (plane beach) and relatively small tidal fluctuations, they will not always be directly applicable to the field, although higher-order solutions can be further explored to overcome some of these shortcomings. Different approaches are necessary for aquifer systems where the simplifying assumptions do not apply, e.g., using numerical simulations that permit consideration of layered or randomly heterogeneous aquifers (e.g., Trefry, 1999; Trefry and Bekele, 2004), or the more complex boundary conditions along the beach (Ataie-Ashtiani et al., 1999b).

Since Henry (1964) developed an analytical solution for a particular salt-water intrusion problem, much discussion and modification of analytical and numerical solutions have been presented. Bear et al. (1999) reviewed recent progress on saltwater intrusion in coastal aquifers, including field studies, theories, analytical solutions and numerical analyses of real cases. Two kinds of approaches have been applied in the numerical simulation of salt-water intrusion: the sharp interface and dispersed inter-face approaches. While mixing between fresh groundwater and seawater is not considered in the former approach, it is incorporated by the latter. Cartwright et al. (2004) studied the oscillation of the salt-freshwater interface due to a wave-induced ground-water pulse using an analytical model based on the sharp-interface assumption. Using a modified version (Ataie-Ashtiani et al., 1999b) of SUTRA (Voss, 1984), Ataie-Ashtiani et al. (1999a) studied the effect of tidal oscillations on seawater intrusion in coastal aquifers based on the dispersed interface approach. It was noted that the effect can be significant on near-shore groundwater hydrodynamics and salt-water intrusion, especially for a low-relief beach.

Submarine groundwater discharge (SGD) has been recognised as an important factor influencing the near-shore environmental ecology for over a decade (Simmons, 1992; Moore, 1996). Field studies have shown that a variety of contaminants can be discharged to estuaries through groundwater, i.e., nutrients and pesticides from agricultural land, organic matters from residential septic tanks and trace metals from industrial landfills (Weiskel and Howes, 1992; Buddemeier, 1996; Gallagher et al., 1996; Robinson et al., 1998). Li et al. (1999) established a theoretical model of mass transport with SGD including the influence of waves and tides. Kaleris et al. (2002) simulated the net groundwater discharge to the sea using MODFLOW (McDonald and Harbaugh, 1998). Uchiyama et al. (2000) considered the effect of tidal fluctuations on SGD in a combined field and numerical modelling study.

As most studies investigated separately the aforementioned three topics, it is now appropriate to combine the tidal influence on groundwater dynamics, salt-water intrusion and chemical transport in a coastal aquifer model to elucidate their interactions. Moreover, since previous research has shown that the beach slope is a vital factor influencing coastal aquifer water table fluctuations and salt-water intrusion, and given the common occurrence of low-relief estuaries, the study will consider particularly the effect of tidal fluctuations at a mildly sloping beach. For this purpose, a field site at Ardeer, Scotland, was monitored and analysed. In this paper, using the numerical simulations based on the field data, the effect of tidal fluctuations on groundwater dynamics, salt-water intrusion and contaminant transport in the

coastal aquifer were explored. Then, the effect of beach slope was examined by comparing simulations of sloping and vertical beaches.

2. Field Monitoring and Analysis

2.1. Site settings

Ardeer, near Irvine Bay in north Ayrshire, Scotland, is a former industrial site containing a substantial waste deposit as a result of a century of waste disposal. The buried waste has generated subsurface leachate into the coastal aquifer. There are different types of wastes at the site, which are concentrated in several places.

The study area is located on the west bank of the Garnock River (Figure 1), where a major source of acidic contamination has been located about 100 m from the riverbank, near bore SW2 (Figure 2). The low-relief estuary has a mildly sloping sandy beach. Between low and high tide the beach width varies by 180 m. The main groundwater flow path is towards the estuary. Given the proximity of the estuary to the landfill/site configuration, leachate would inevitably migrate toward the open water and possibly threaten the estuarine ecosystem, although monitoring shows that there is no contamination reaching the estuary.

There is no extraction of groundwater from the aquifer. The vertical groundwater flux is mainly from rainfall recharge, evaporation and transpiration. In the beach area the water table is less than 0.5 m under the sand while the inland area is mostly grassland with the groundwater depth greater than 2 m. This difference in the depth to the water table is expected to lead to differences in groundwater recharge due to, for example, increased evapotranspiration from the shallower parts of the water table. Outflow occurs via the large seepage face on the estuary shore and also through groundwater discharge in the sub-tidal area.

Field monitoring was performed to characterise the tidal influence on the groundwater dynamics as well as the salt-water intrusion. Water table monitoring was carried out along the cross section I-I (Figure 2), which is almost perpendicular to the estuary. The boreholes are Al01 (furthermost from the estuary), Mid-estuary, with Bh4 and Beach in between.

Salt-water intrusion and infiltration to the coastal aquifer were monitored through measurements of pore water electrical conductivity (EC) and chloride concentration. Three multi-level samplers (MLS01, MLS02 and MLS03) were set up in the cross-section II-II, which is near and almost parallel to cross-section I-I (Figure 2). The EC values of water samples from MLS01, MLS02 and MLS03 were obtained and converted to salinity. Additional shallow boreholes were hand-dug directly on the beach face for additional EC measurements.

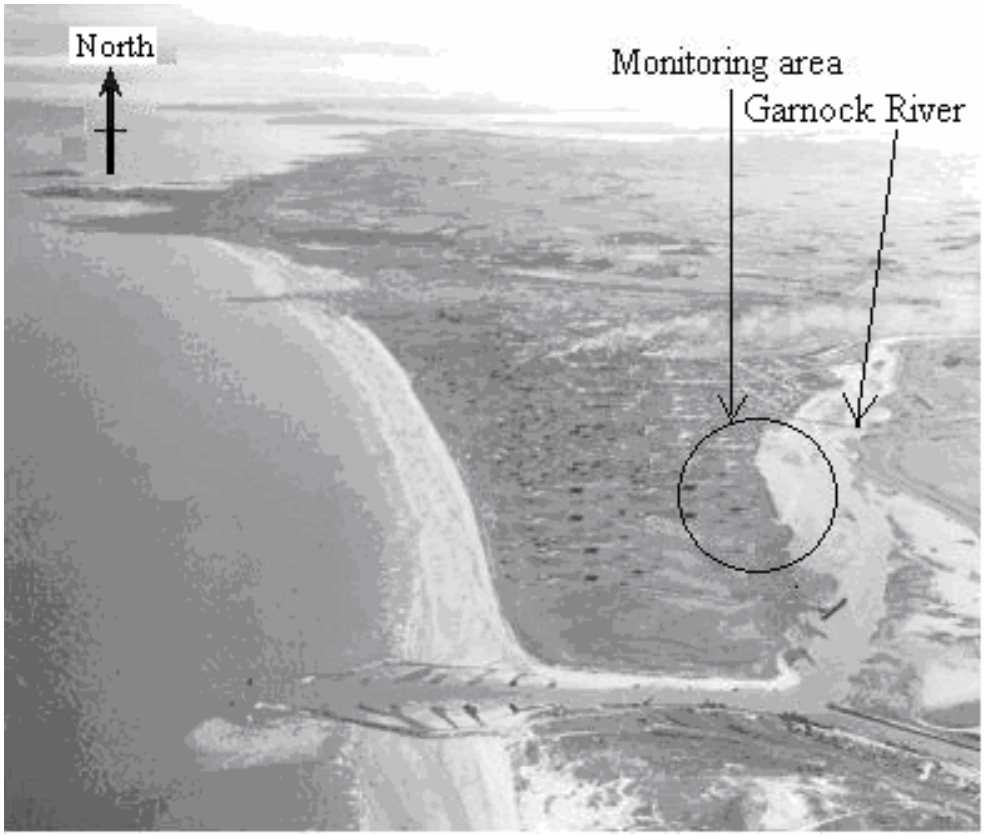

Figure 1: Location of the Ardeer site – a coastal aquifer adjacent to a low-relief estuary.

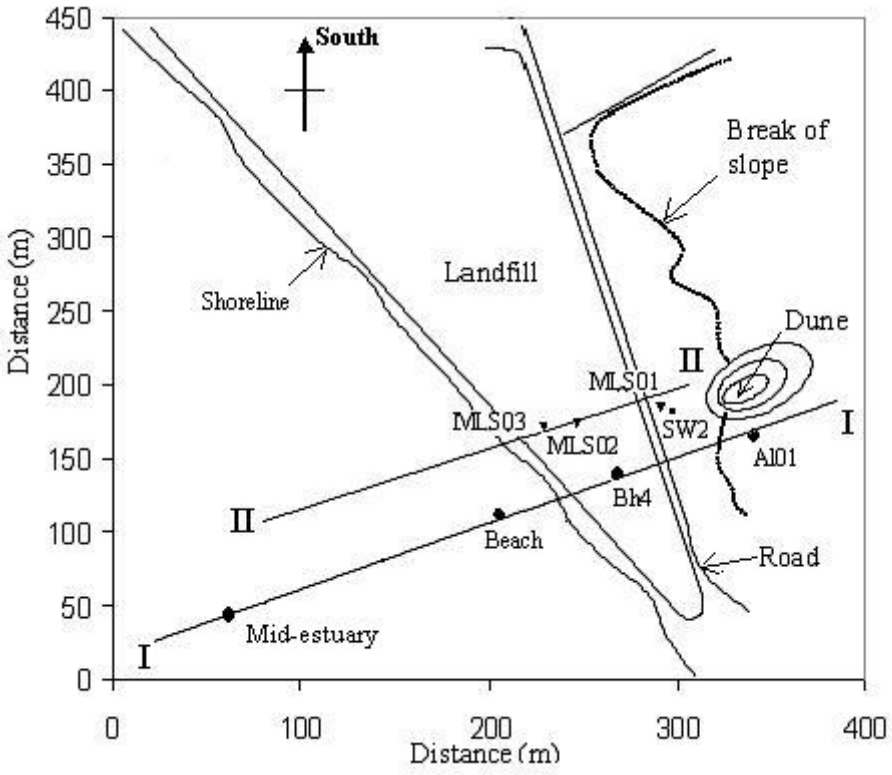

Figure 2: Sketch map of the study area and field monitoring design. Locations of monitoring wells are marked (Al01, SW2, MLS01, MLS02, MLS03, Bh4, Beach and Mid-estuary).

2.2. Field observations

The hydraulic properties of the coastal aquifer near the estuary were obtained from borehole geological logs, grain-size analysis and borehole dilution tests. It was concluded that the unconfined aquifer is composed of successive layers of river and marine alluvial sand and gravel, with intermittent clay lenses as shown in Figure 3. Note that the elevation shown in all the figures in this paper is the elevation above Ordnance Datum (Newlyn, UK). A boulder clay layer located at approximately 15 m below the ground surface acts as an aquitard.

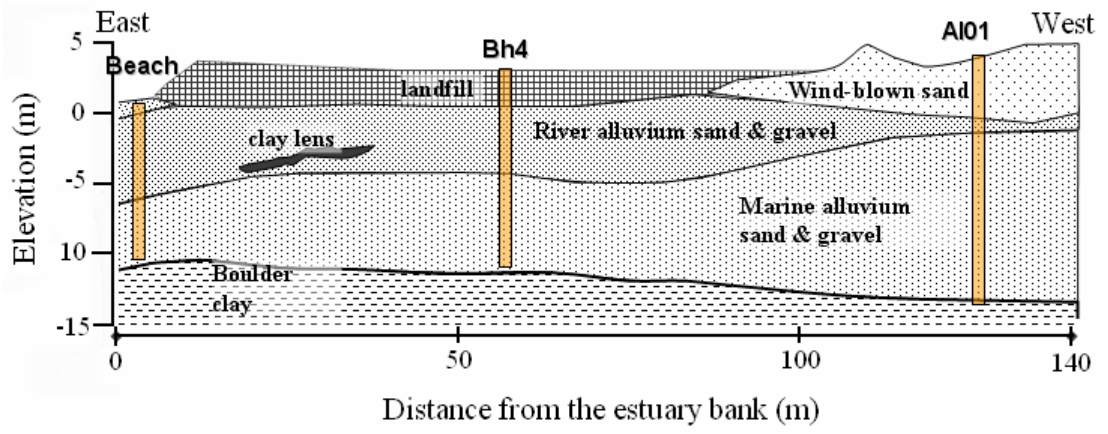

Figure 3: The geological structure along the cross section between the Beach bore and the Al01 bore.

Table 1. Salinity of the water under/on the beach.

Distance from the Mid-estuary (m)	54.6	109.9	131.6	147.7	163.8	174.3	182
Depth under the beach surface (m)	0	0	0.05	0.1	0.2	0.3	0.5
Salinity (g l^{-1})	17.78	11.13	16.32	15.82	8.96	16.23	14.56

Salinity of the water just beneath the beach surface is nearly 50% that of normal seawater (Table 1), which indicates mixing of infiltrated seawater and the discharging groundwater. Along the MLS transect (II - II), the salinity (Figure 4) is higher towards the lower part of the aquifer, possibly resulting from density-driven salt-water intrusion. There is also considerable salinity in the upper part of MLS02, most likely the result of contaminant transport near/at surficial depths. High salinity is found at large depths for MLS01 which is about 280 m away from the Mid-estuary bore. As salt-water intrusion to this location is unlikely, this might be the result of ancient water remaining in pores of finer sediments.

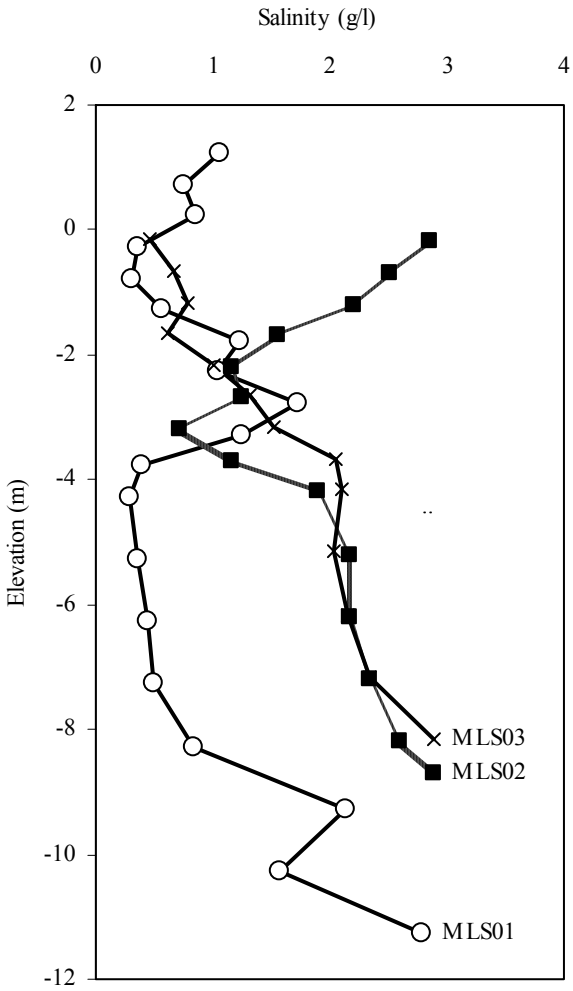

Figure 4: Vertical salinity distribution at MLS01, MLS02 and MLS03.

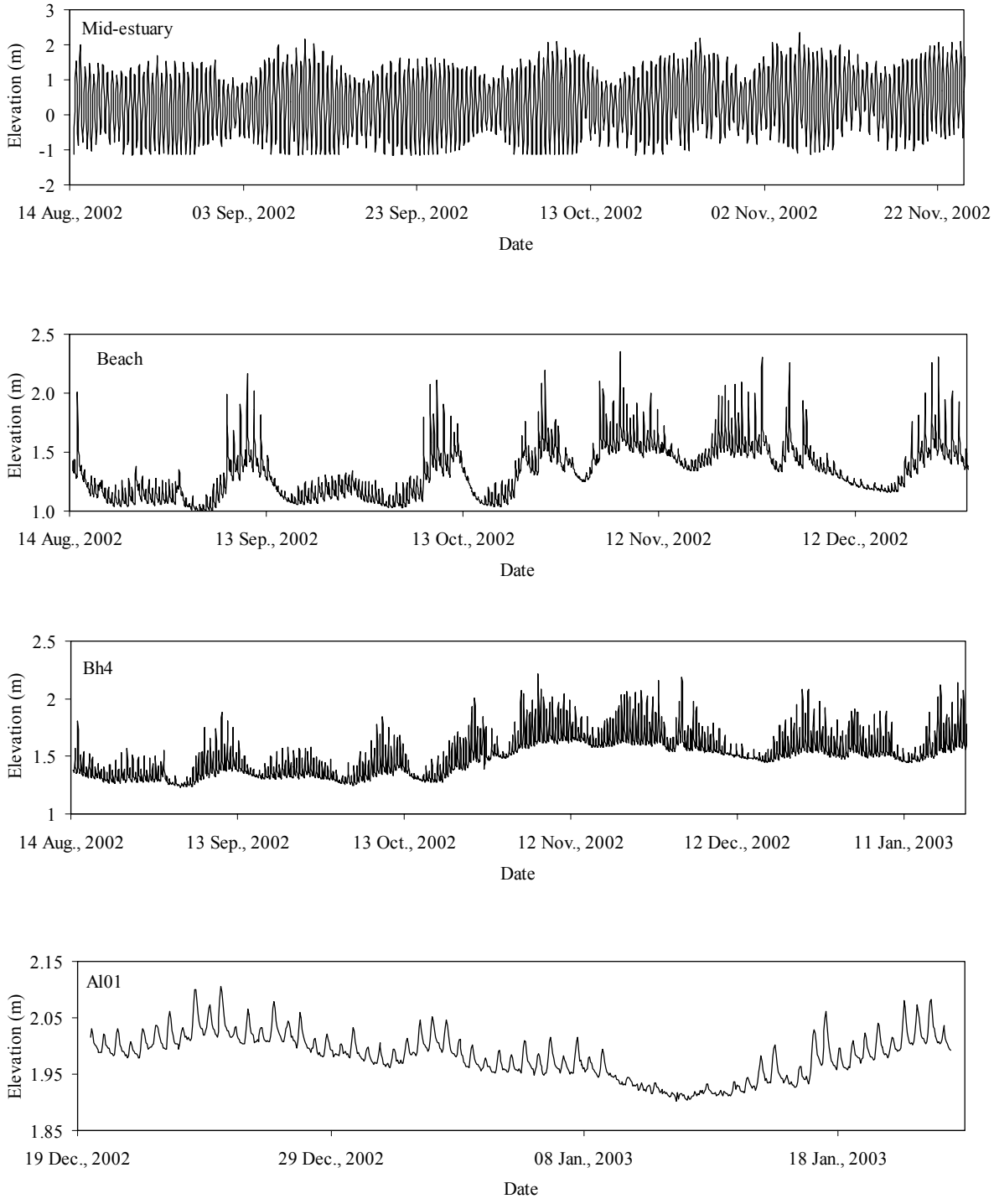

Figure 5: Monitored water table fluctuations in four monitoring bores.

The measured water table fluctuations in transect I-I are shown in Figure 5 for the period from August 2002 to January 2003. Clearly, the aquifer is greatly influenced by tidal loading.

The estuarine tide includes multiple frequencies such that a detailed analysis of water head data is necessary to resolve the aquifer-estuary relationship.

2.3. Tidal frequency analysis

Data collected in the cross section I-I (Figure 2) were subjected to Fourier analysis using the Fast Fourier Transform (FFT) function in MATLAB. The results, given in Figure 6a, show that the dominant period/frequency for the Mid-estuary borehole is 0.52 d/1.94 d^{-1} (M2, lunar semi-diurnal constituent), followed by 0.50 d/2.0 d^{-1} (S2, solar semi-diurnal constituent) and 1.08 d/0.93 d^{-1} (O1, lunar diurnal constituent). Figure 6b shows the results of the phase analysis at the given dominant periods/frequencies. Note that additional data (3s, as numbered in the figure caption), extracted from the Bh4 dataset, was added to the figure to give all datasets the same starting time. While the starting time for the Al01 dataset is different from those in the other three boreholes (see the notes in Figure 6), we create dataset (3s) to calibrate the phase shift obtained for Al01. Figure 7 shows the amplitude damping and phase shift for the dominant signal M2 based on the FFT analysis. Here the phase value of Al01 is calculated from the data in Figure 6b, using the value in dataset (4) minus the value in (3s) plus the value in (3). When the fluctuations propagated inland, the amplitude of semi-diurnal signal M2 decayed exponentially with a linearly increasing phase lag, in accordance with the field observations of Erskine (1991). However, the trend of amplitude damping and phase shift for the Beach and Bh4 bores is not so clear, possibly due to the hydrogeological heterogeneity in this area leading to different tidal impacts along the river flow direction. Another possibility is along-shore flow interacting with the cross-shore transmission of the tidal signal (Li et al., 2000b). The calculated tidal frequencies were used in an analytical solution (Jeng et al., 2005b), which models tide-induced beach water table fluctuations in a sloping coastal aquifer. Results show reasonable agreement with the monitored data for this particular aquifer.

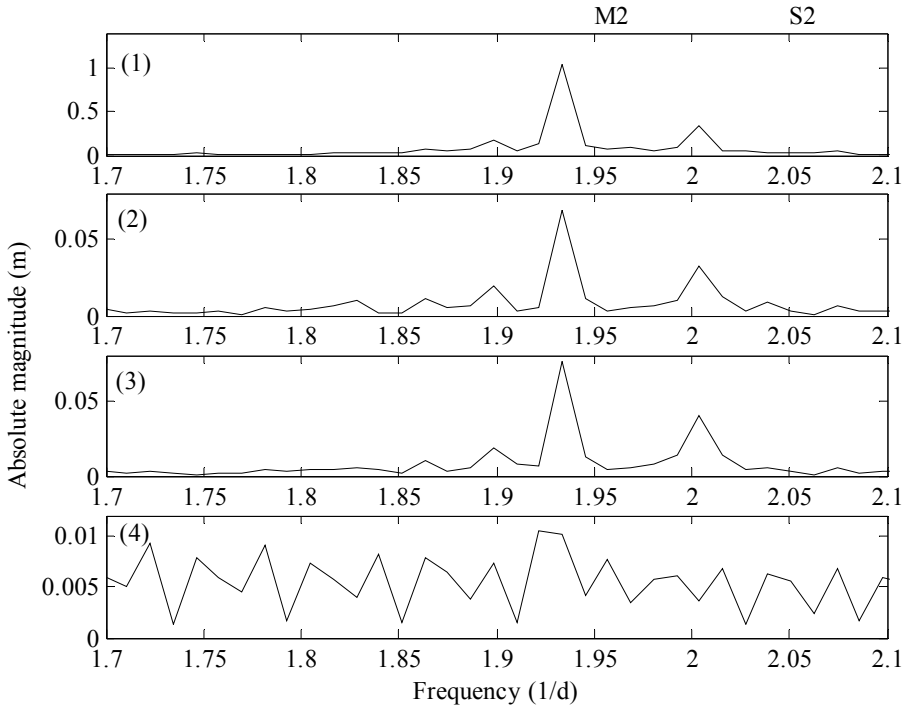

(a)

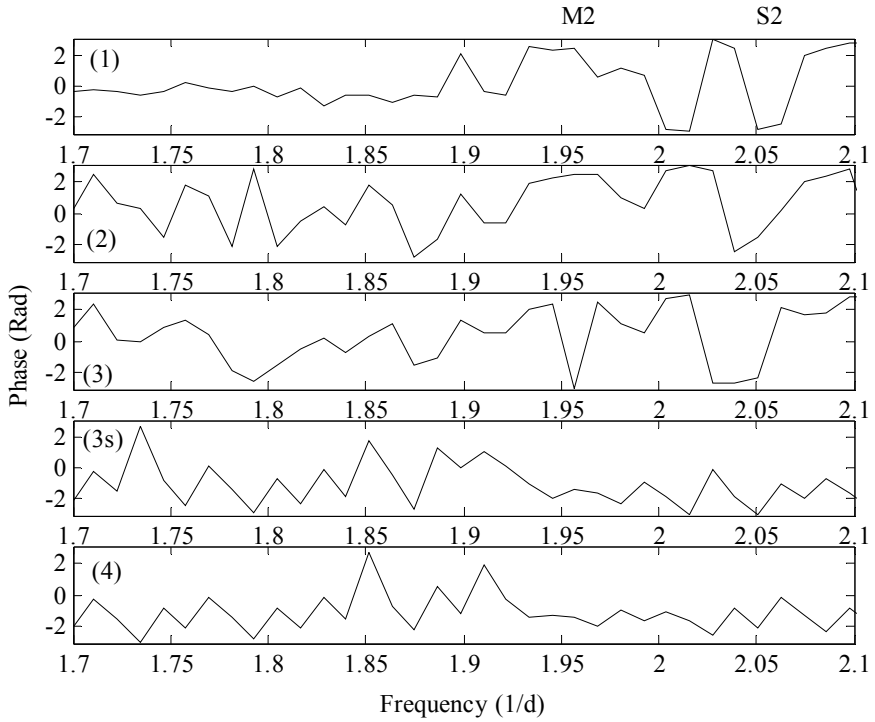

(b)

Figure 6: Fast Fourier Transform (FFT) analysis of the water table in the 4 bores: (a) Absolute value at different frequencies; (b) Phase at different frequencies, with (1) Mid-estuary FFT analysis based on a 2480-h time series starting at 11:00 14 August 2002; (2) Beach FFT analysis based on a 3301-h time series starting at 11:00 14 August 2002; (3) Bh4 FFT analysis based on a 3866-h time series starting at 11:00 14 August 2002; (3s) Bh4 FFT analysis based on a 865-h time series starting at 12:00 19 December 2002; and (4) Al01 FFT analysis based on a 816-h time series starting at 12:00 19 December 2002.

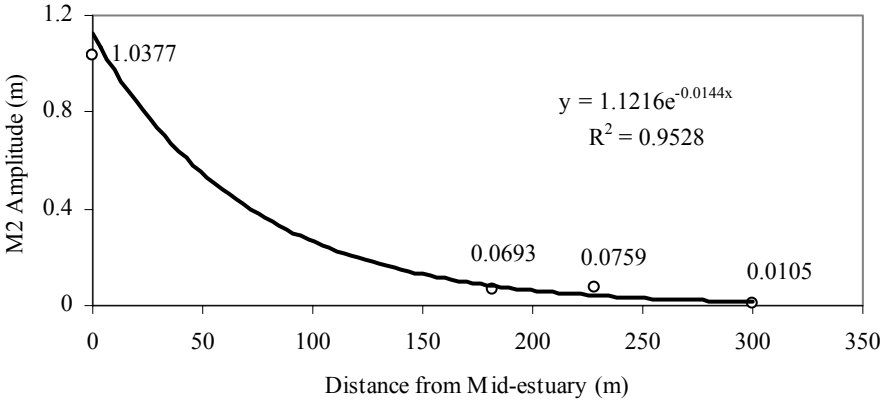

(a)

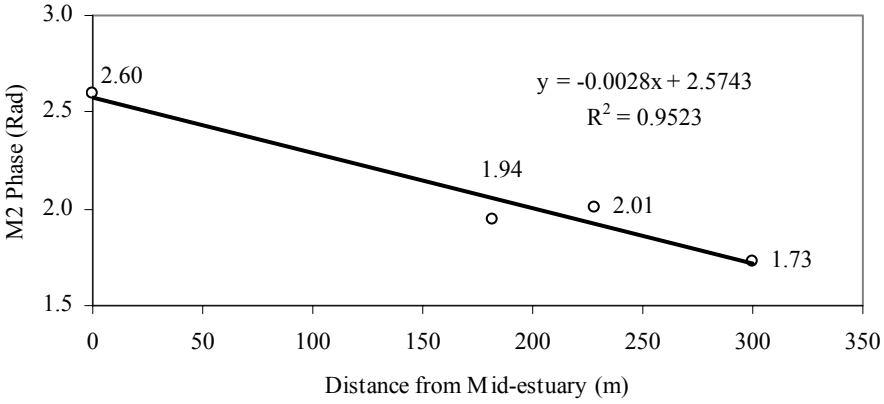

(b)

Figure 7: Amplitude and phase variations of M2 from FFT analysis along the cross section I-I: (a) amplitude variation; (b) phase variation.

3. Mathematical Models

3.1. Analytical solution

In this study, the flow is assumed to be homogeneous and incompressible in a rigid porous medium. The configuration of the groundwater flow in the coastal aquifer is shown in Figure 8. In the figure, $h(x,t)$ is the total tide-induced water table height, D is the thickness of the aquifer and β is the beach slope. Seepage face effects are ignored. Since the fluid is incompressible, the free surface flow of groundwater satisfies the conservation of mass, leading to Laplace's equation (e.g., Bear, 1972):

$$\frac{\partial^2 \phi}{\partial x^2} + \frac{\partial^2 \phi}{\partial z^2} = 0, \qquad (1)$$

where ϕ is the potential head.

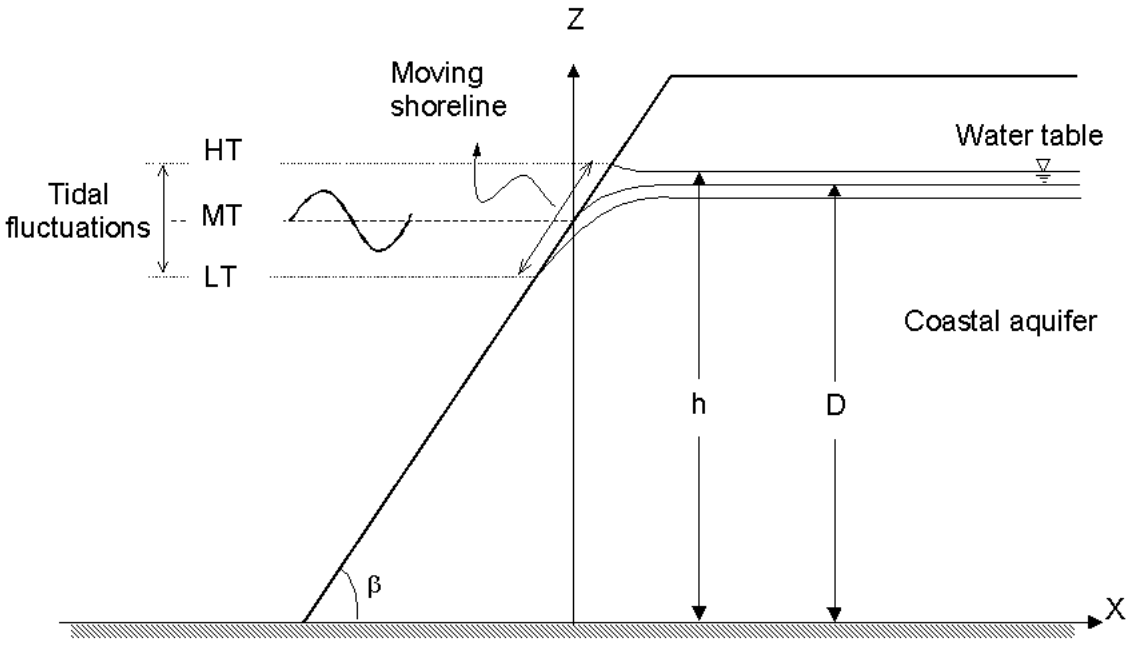

Figure 8: Sketch of tidal dynamics in coastal aquifers.

Equation (1) is to be solved subject to the following boundary conditions,

$$\frac{\partial \phi}{\partial z} = 0, \qquad \text{at } z = 0, \qquad (2a)$$

$$\phi = h, \qquad \text{at } z = h, \qquad (2b)$$

$$n_e \frac{\partial \phi}{\partial t} = K\left[\left(\frac{\partial \phi}{\partial x}\right)^2 + \left(\frac{\partial \phi}{\partial z}\right)^2\right] - K\frac{\partial \phi}{\partial z}, \qquad \text{at } z = h, \qquad (2c)$$

$$h(x_0, t) = D + A_1 \cos(\omega_1 t + \delta_1) + A_2 \cos(\omega_2 t + \delta_2)$$

$$\text{at } x_0 = \left[A_1 \cos(\omega_1 t + \delta_1) + A_2 \cos(\omega_2 t + \delta_2)\right]\cot\beta, \qquad (2d)$$

$$\frac{\partial \phi}{\partial x} \to 0, \qquad \text{as } x \to \infty. \qquad (2e)$$

Note that the soil properties are defined by the soil porosity (n_e) and hydraulic conductivity (K).

Following Teo *et al.* (2003), the tide-induced water table fluctuation can be expressed as

$$h(x,t) = D\left[1 + \left(\alpha H_{01} + \alpha^2 H_{02}\right) + \varepsilon\left(\alpha H_{11} + \alpha^2 H_{12}\right) + +\varepsilon^2 \alpha H_{21}\right] \quad , \qquad (3)$$

where $\varepsilon = \sqrt{\frac{n_e \omega_1 D}{2K}}$ is the shallow water parameter and $\alpha = \frac{A_1}{D}$ is the amplitude parameter. Detailed derivation of the analytical solutions and H_{ij} coefficients are available in Appendix

3.2 Comparisons with field data

To test the analytical solutions, field data of water table fluctuations at Ardeer, Scotland,is used as an example. Ardeer is a former industrial site containing a substantial waste deposit. The low-relief estuary adjacent to the site has a mildly sloping sandy beach. Between low and high tide the beach length varies by 180 m. Field monitoring was conducted to characterize the tidal influence on the ground-water dynamics and contaminant migration as well as the salt-water intrusion. Detailed information on the field observations is given in Section 2.

Analysis on tidal signals shows that the fluctuation amplitude decreases exponentially with distance from the estuary, accompanied by a phase lag, as has been shown by the FFT analysis of the observed data [Section 2]. FFT analyses of the estuarine tides have shown the dominant frequencies are M2, S2 and O1. To simplify the analytical solution, we only considered M2 and S2 components. The fitted expression modeling the estuarine tides is:

$$h(x,t) = D + 1.1745\cos(\omega_1 t - 1.6676 + \frac{\pi}{2}) + 0.08\cos(\omega_2 t - 1.3377 + \frac{\pi}{2}), \qquad (4)$$

where h is measured in meters, $\omega_1 = 2\pi / 0.52$ rad/day and $\omega_2 = 4\pi$ rad /day.

The calculated groundwater table fluctuation based on the analytical solution with the above estuarine tide is shown in Figure 9 where the damping of the amplitude is compared against observed data. In the development of the analytical solutions, we assume the coastal aquifer is homogeneous with a uniformly sloped beach. However, the real aquifer is multi-layered and inhomogeneous in both vertical and horizontal direction near the intersection of the ocean and the aquifer. It has been reported that inhomogeneity will affect water table fluctuations (Trefry, 1999). Furthermore, the variations of beach slope are expected to affect the water table level, but no solution is available yet. In addition, seepage face effects have been ignored. Finally, we consider two main frequencies of tidal waves (M2 and S2) in equation (4), based on FFT analysis. The inclusions of other tidal components may improve the prediction of the analytical solutions.

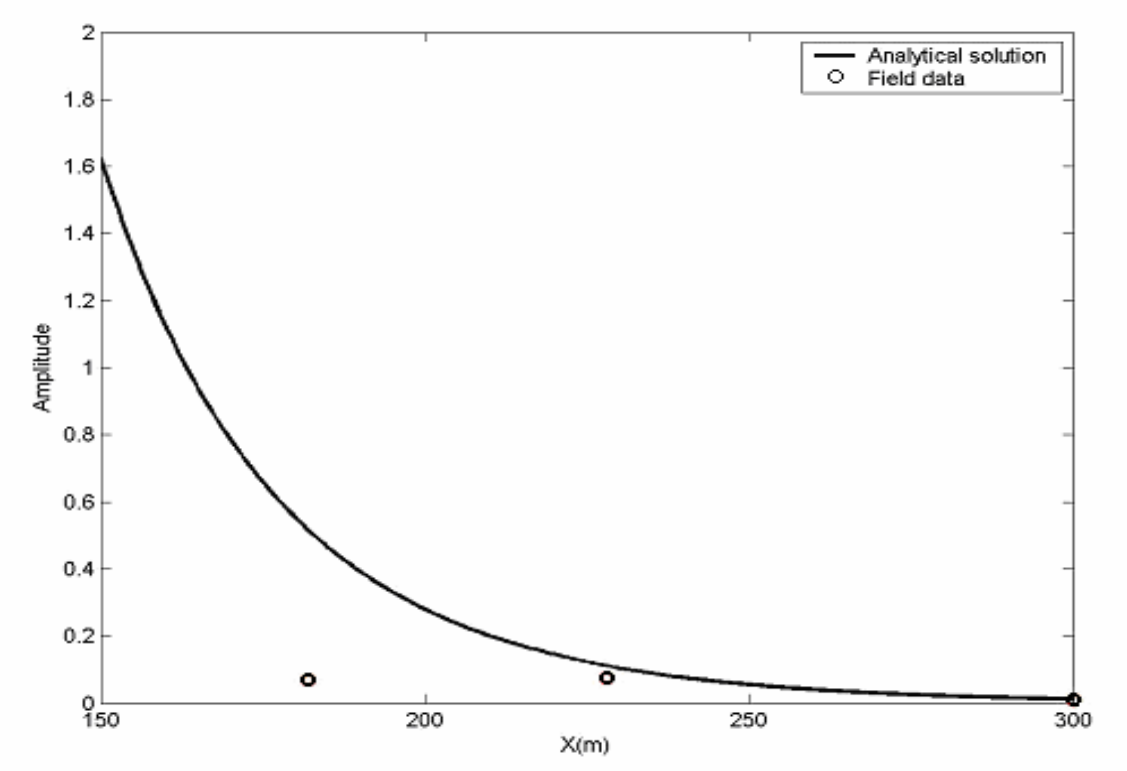

Figure 9: Comparison of analytical solution with field data.

3.3 Parametric study

The major difference between the present solution and previous solution [*Li et al*. 200b] is the higher-order component. It is of interesting to examine the effects of higher-order component here. The input data for the comparison is listed in Table 2. As seen in Figure 10, the previous solution [*Li et al.*, 2000b] overestimates the water table elevation.

Table 2 Input data for Figures 10-13.

Soil porosity (n_e)	0.22
Hydraulic conductivity (K) (m/day)	50
Slope of the beach (β) (rad)	0.02
Thickness of aquifer (D) (m)	5
Amplitude of the first tidal wave (A_1) (m)	2
Frequency of the first tidal wave (ω_1)	4π
Amplitude parameter (ε)	0.372
Shallow water parameter (α)	0.2

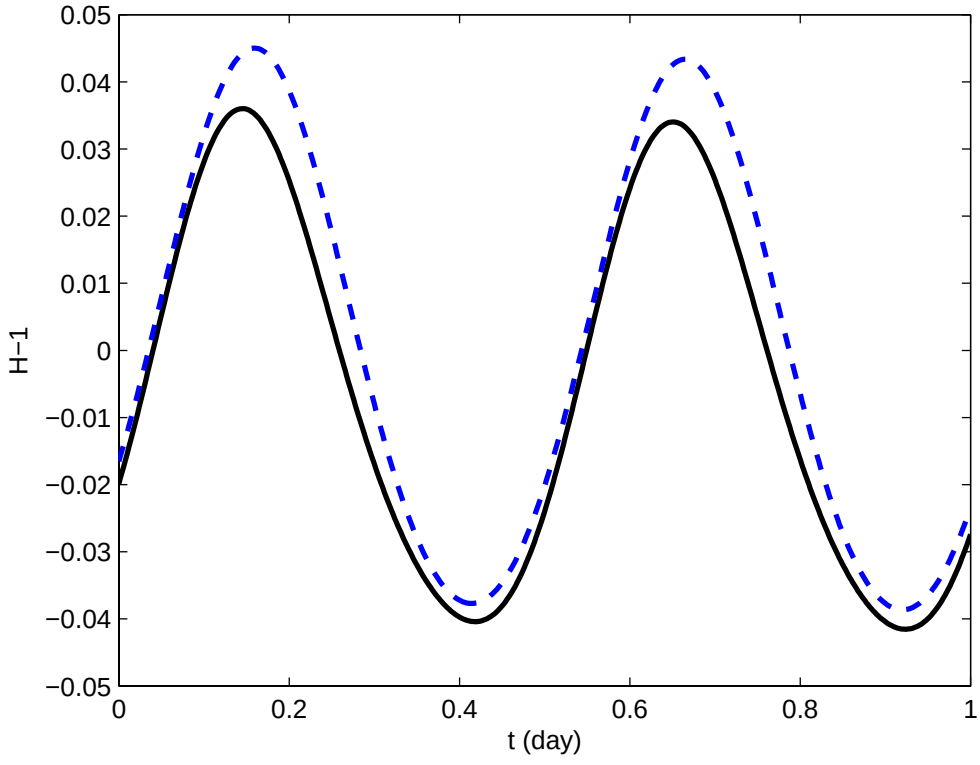

Figure 10: Effects of higher-order components on water table fluctuations in coastal aquifers (solid lines =the present solution and dashed lines=*Li et al.* [2000b]). [X_1=2, λ = 0.5, ω = 0.5, and (δ_1,δ_2) = (0,0)]

As shown in analytical solutions presented in section 2, numerous parameters are involved in the solutions. The objective of this parametric study is to investigate three parameters. These are:

- Amplitude ratio ($\lambda = A_2/A_1$)
- Frequency ratio ($\omega = \omega_2/\omega_1$)
- Phases (δ_1 and δ_2)

Although spring-neap tides normally have the frequencies ration (ω) close to unity, the variation of frequency ration (ω) is also considered here for the general applications of other cases rather than limited to spring-neap tides. Recently, Li et al. [2000b] discussed part of the above parameters briefly based on Boussinesq equation, it is worthwhile to re-examine the effects of eth above parameters with the new solution presented in section 2. The input data of numerical examples is given in Table 2.

The amplitude ratio (λ) is the ratio of the amplitudes of two tidal components (A_2/A_1). Here we allow λ to vary from zero (0) to unity (1). $\lambda = 0$ represents the case without the second tidal component, which is the case reported in Teo *et al*. [2003], while $\lambda = 1$ represents the case of equal weight of two tidal signals.

Figure 11 illustrates the effects of the amplitude ratio (λ) on the tide-induced water table height above the mean thickness of aquifer at $T = 0$, i.e., $H - 1 = (h - D)/D$. As shown in the figure, the water table height increases as the amplitude ratio (λ) increases, i.e., it increases as the amplitude of the second tidal signal increases.

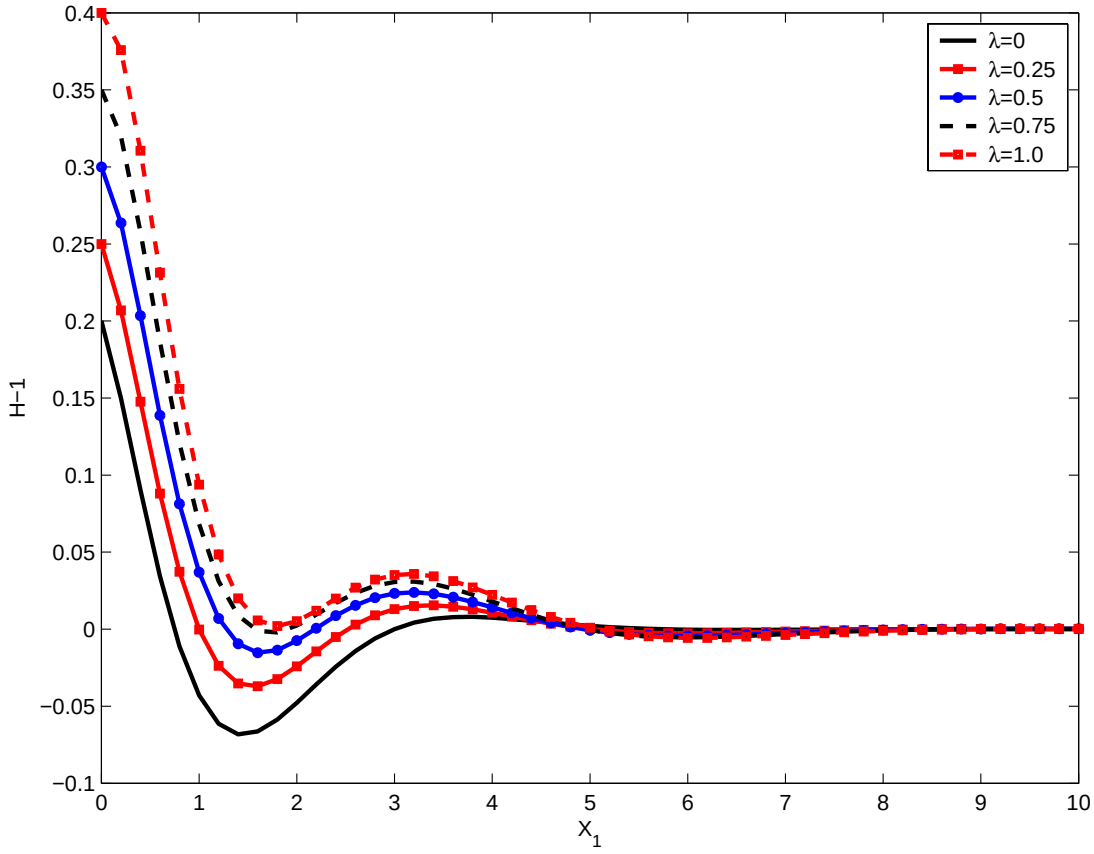

Figure 11: Effects of amplitude ratio (λ) on water table fluctuations in coastal aquifers. [ω = 0.5, and $(\delta_1,\delta_2) = (0,0)$, $t=0$.]

Besides the amplitude ratio (λ), the frequency ratio (ω) is another factor, which may affect the tide-induced water table fluctuations. The distribution of water table heights versus the horizontal distances (X) for various values of frequency ratio (ω) is presented in Figure 12. As shown in the figure, the water table height decreases as ω increases when $X < 1.8$. When X increases (X>1.8), the influence of ω perform an irregular trend, which may require more advanced theories.

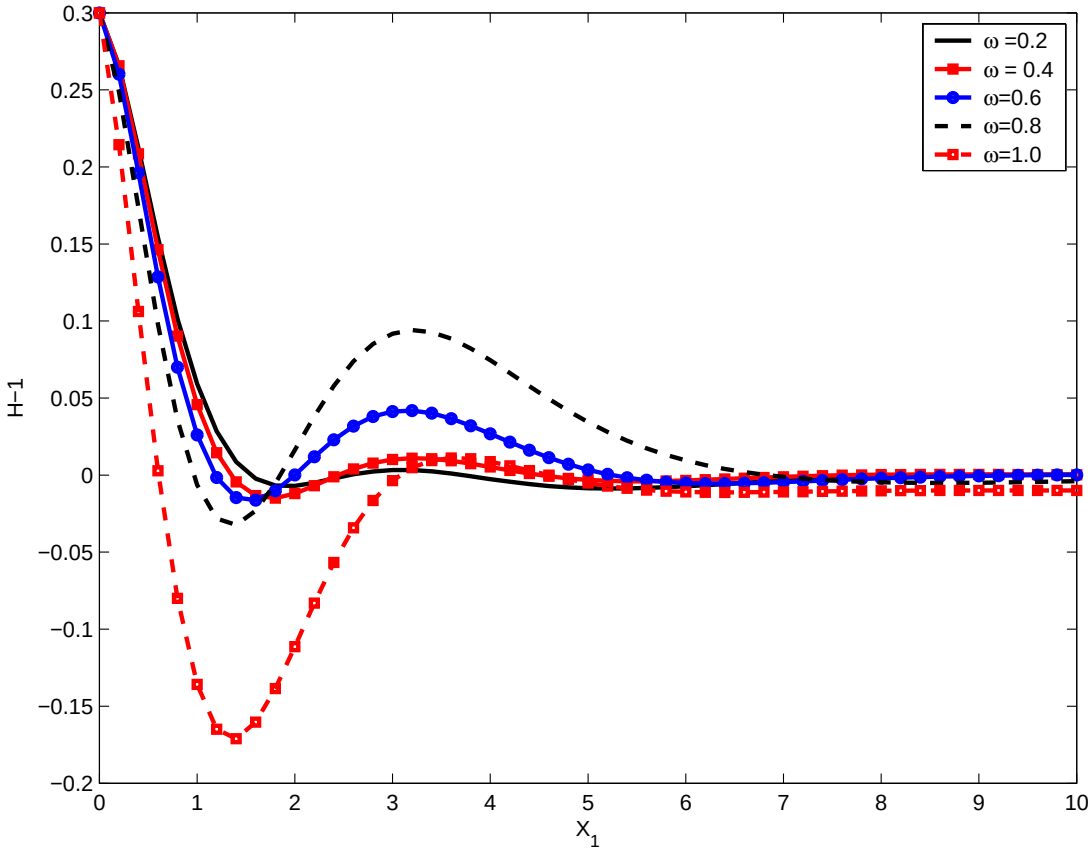

Figure 12: Effects of frequency ratio (ω) on water table fluctuations in coastal aquifers. [$\lambda = 0.5$ and $(\delta_1,\delta_2) = (0,0)$, $t=0$].

Another major difference between the previous solution [Teo *et al.*, 2003] and the present solution is the phase differences between two tidal signals. Figure 13 illustrates the effects of phase differences of two tidal components on the tide-induced water table heights. To see the influence of phase difference, we fix $\delta_1 = 0$, and vary δ_2 from zero (0) to π. Generally speaking, the phase difference significantly affects the water table height. For example, the water table height decreases as $\delta_2 - \delta_1$ increases.

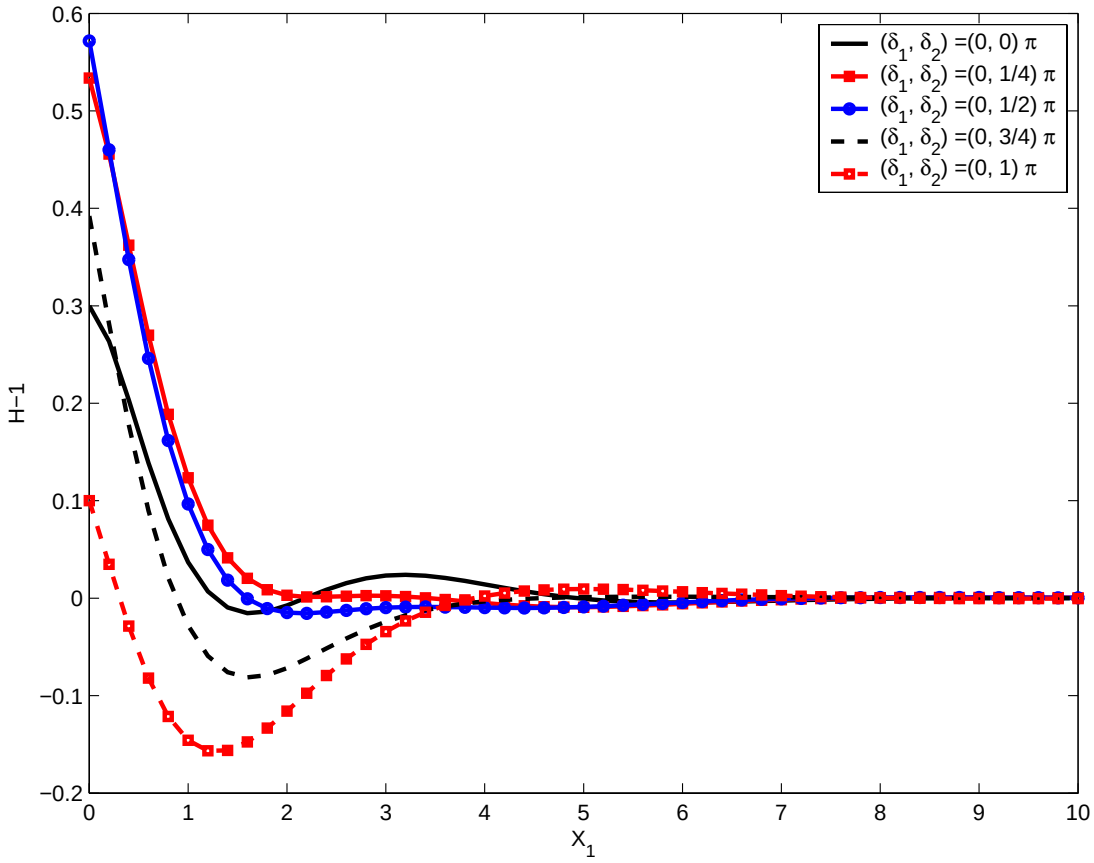

Figure 13: Effects of phases (δ_1 and δ_2) on water table fluctuations in coastal aquifers. [$\lambda = 0.5$, $\omega = 0.5$, $t=0$]

4. Simulation Using SEAWAT-2000

4.1. Mathematical basis and model introduction

A model capable of multi-species transport with density-dependent flow is required to simulate the tidal influence on groundwater hydrodynamics, salt-water intrusion and chemical transport. SEAWAT-2000 (Langevin et al., 2003) was chosen to perform this simulation. It couples MODFLOW-2000 and MT3DMS, and takes into account the effect of density on groundwater flow. With the tidal fluctuations over a mildly sloping beach, the cells near the groundwater surface will experience temporally varying saturation changes. SEAWAT-2000 (and MODFLOW-2000) has a drying/rewetting function to simulate variable saturation although it does not model directly the unsaturated flow.

Guo and Langevin (2002) presented the governing equation for variable-density groundwater flow in an anisotropic medium. For this study, isotropic and heterogeneous conditions apply, in which case the governing flow equation is,

$$\frac{\partial}{\partial x_i}\left[\rho K_f\left(\frac{\partial h_f}{\partial x_i}+\frac{\rho-\rho_f}{\rho_f}\frac{\partial Z}{\partial x_i}\right)\right]=\rho S_f\frac{\partial h_f}{\partial t}+\theta\frac{\partial \rho}{\partial t}-\rho_s q_s, \quad (5)$$

where x_i [L] is the i^{th} orthogonal coordinate; K_f [LT^{-1}] is the hydraulic conductivity, h_f [L] is the freshwater head, ρ [ML^{-3}] is the fluid density, S_f [L^{-1}] is the equivalent freshwater specific storage, θ is the effective volumetric porosity, and ρ_s [ML^{-3}] and q_s [T^{-1}] represent the density and flux of the source/sink.

Multi-species transport with advection and dispersion is modelled using (e.g., Zheng and Wang, 1999)

$$\frac{\partial\left(\theta C^k\right)}{\partial t}=\frac{\partial}{\partial x_i}\left(\theta D_{ij}\frac{\partial C^k}{\partial x_j}\right)-\frac{\partial}{\partial x_i}\left(\theta v_i C^k\right)+q_s C_k^s+\sum R_n, \quad (6)$$

where C^k [ML^{-3}] is the concentration for dissolved species k, D_{ij} [L^2T^{-1}] is the hydrodynamic dispersion tensor, v_i [LT^{-1}] is the groundwater pore velocity, C_k^s [ML^{-3}] is the concentration of species k from the source/sink and R_n [$ML^{-3}T^{-1}$] is the reaction term.

4.2. Simulations of Groundwater Fluctuation, Saltwater Intrusion and Chemical Transport at the Ardeer Site

4.2.1. Introduction to the model design

Using SEAWAT-2000, contaminant/salt transport with density-dependent flow was simulated for the Ardeer site. The cross section I-I (Figure 2) was chosen as the simulation domain assuming negligible flow perpendicular to this cross section. Water table fluctuations were monitored in several bores along this section. As mentioned above, based on the field data (Figure 3), the flow domain along the cross section was divided into several zones having different hydrogeological properties (Figure 14 and Table 3). Domain discretisation (grid sizes) aimed to capture the morphology of the beach and maintain acceptable accuracy of the simulations with manageable computational costs (Figure 4).

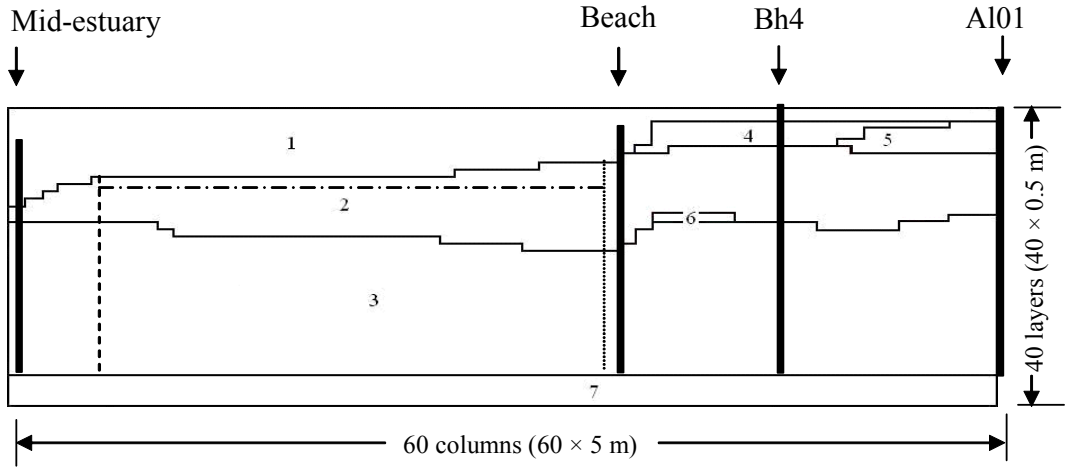

Figure 14. Zone classification and grid division for the numerical model simulation: (1) free surface water body/atmosphere; (2) river alluvium (sand); (3) marine alluvium (sand); (4) wind-blown sand; (5) waste layer; (6) thin clay layer; (7) clay (aquitard). (Dashed lines are to help explain calculations in Section 4.3)

Table 3. Hydrogeological properties of the aquifer used in the simulations.

Zone number[a]	1	2	3	4	5	6	7
Hydraulic conductivity (m d^{-1})	86400	170	100	35	75	1	0.01
Effective porosity	1	0.22	0.22	0.22	0.22	0.22	0.22
Specific yield	1	0.04	0.04	0.04	0.04	0.04	0.04
Specific storage (m^{-1})	0.00001	0.000005	0.000005	0.000005	0.000005	0.000005	0.000005
Longitudinal dispersivity (m)	10	1	1	1	1	1	1

[a] The zone divisions and zone numbers are shown in Figure 14.

The aquifer was assumed to be filled with fresh groundwater initially, followed by a simulation of salt-water intrusion for nearly 10 y (3554 d). In the first 1719 d, the aquifer was subject to fresh groundwater discharge and salt-water intrusion, with a fixed salt-water head (the averaged tidal water head, 0.515 m, for the monitoring period) applied at the estuary boundary (Mid-estuary) and a constant water head (1.98 m, which is the averaged value over the monitoring period) applied at the landward boundary (Al01). At the end of 1719 d, the groundwater flow and salt-water intrusion had reached steady state, according to the simulation results. Then, a conservative contaminant plume was assumed to be generated from the inland area (30 m from Al01, near the position of bore SW2 where the real acidic leachate plume is produced). The simulation ran for another 5 y (1825 d). After that, the tidal oscillation (using the observed data from 19 – 29 December 2002) was switched on and the simulation continued for 10 d, including the influence of tidal fluctuations, density-dependent flow and the transport of the contaminant plume (Table 4).

Table 4. Boundary condition and other information for each simulation stress period

Model period	Boundary condition				Other information	
	Water flow		Solute transport		Salt water intrusion	Contaminant transport
	Inland boundary	Estuarine boundary	Inland boundary	Estuarine boundary		
0-1718 d	Constant water head	Constant water head	Constant fresh water concentration	Constant seawater concentration[a]	Yes	No
1719-3543 d	Constant water head	Constant water head	Constant fresh water concentration	Constant seawater concentration[a]	Yes	Yes[b]
3544-3554 d	Monitored ground water fluctuations from 19 Dec.2002 to 29 Dec.2002	Monitored tidal fluctuations from 19 Dec.2002 to 29 Dec.2002	Constant fresh water concentration	Constant seawater concentration[a]	Yes	Yes[b]

[a] The seawater concentration varied vertically, with slightly higher concentrations in the deeper part of the aquifer.

[b] The contaminant is generated with a constant concentration about 270 m from the Mid-estuary bore, and with an elevation of about 1 m.

4.2.2. Groundwater table fluctuation and hydrodynamics

The simulated groundwater table fluctuations in bores Beach and Bh4 were compared with the monitored data (Figure 14). In the simulations the rainfall infiltration and evaporation, were ignored. The surface soil layer is highly heterogeneous which would result in spatially and temporally variable recharge rates that could not be captured without detailed field sampling. One possible effect of this neglect is that the water table predictions in the beach area (where the water table is near the surface) will be lower than the measurements. Figure 9a shows that the measured data and model predictions are offset but otherwise are in reasonably good agreement

For both the Beach and Bh04 boreholes, the simulation depicts the asymmetry character (sharp rise and slow decline) in the water table fluctuation as has been noticed previously (e.g., Raubenheimer and Guza, 1999). The peaks are more pronounced in the monitored data than in the simulations. The reasons for this difference could include: (i) incomplete knowledge of the hydrogeological properties and their variations within the aquifer, (ii) coarseness of the grid used in the simulation (height 0.5 m and length 5 m for each cell) and/or (iii) modelling of the tidal flow above the beach using an artificial, very permeable aquifer layer.

For (i) we have considered limited changes to the aquifer heterogeneity but without a much more detailed investigation of the site characteristics are unable to provide definitive conclusions on its effect. Notwithstanding this, the results shown in Figure 9 are not improved by relatively small changes in geological zonation or hydraulic conductivity values assigned to those zones.

In the case of (ii) we recall that SEAWAT-2000 is a finite-difference code and does not include local coordinate mapping to convert the rectangular prism-shaped grid to one that matches the slopes. Our numerical experiments did not reveal any significant changes to the results presented here. So, while using a more refined grid may provide small changes, the issue of how to represent a curvilinear beach profile within SEAWAT-2000 cannot be directly resolved.

Representing the overland beach flow as flow in a highly permeable layer – item (iii) above – is an artifice of somewhat limited realism. We found numerical instability occurred when the hydraulic conductivity contrasts between the artificial layer and the beach become too large. Obviously, this will affect the infiltration and exfiltration rates across the beach face, and so will affect the computed water table fluctuations shown in Figure 14. Ideally, resolution to this problem would involve coupling of SEAWAT-2000 to a surface water flow model. In previous work we have achieved this but without density effects included (Li et al., 2002). As this step was not taken here, the peaks are possibly more smoothed than would be produced by inclusion of a more realistic surface flow model.

Figure 15 shows the overall flow field in the aquifer and individual flow lines for typical high and low tide states. The large magnitude of the flow velocity in the surface free water is evident in Figure 10a. As these flow rates are much larger than those in the aquifer, other arrows in the plot are difficult to discern. In order to show the flow direction clearly, some arrows were added manually to the graph with a size that does not correspond to the velocity magnitude. In the area near Al01 (location shown in Figure 3), the groundwater flowed towards the estuary for both tidal states, oscillating a little in the vertical direction due to tidal fluctuations. In the area around the thin clay layer (Figure 13), the flow lines were sparse, indicating an area of relatively slow flow.

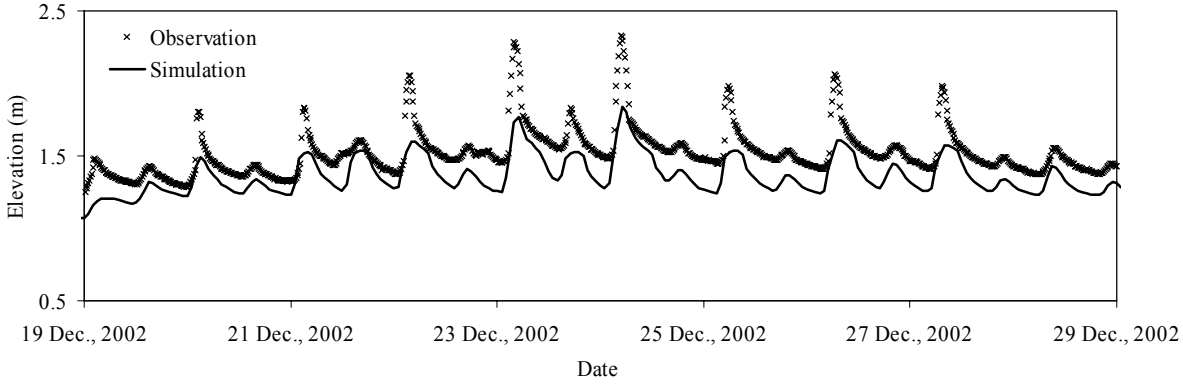

(a)

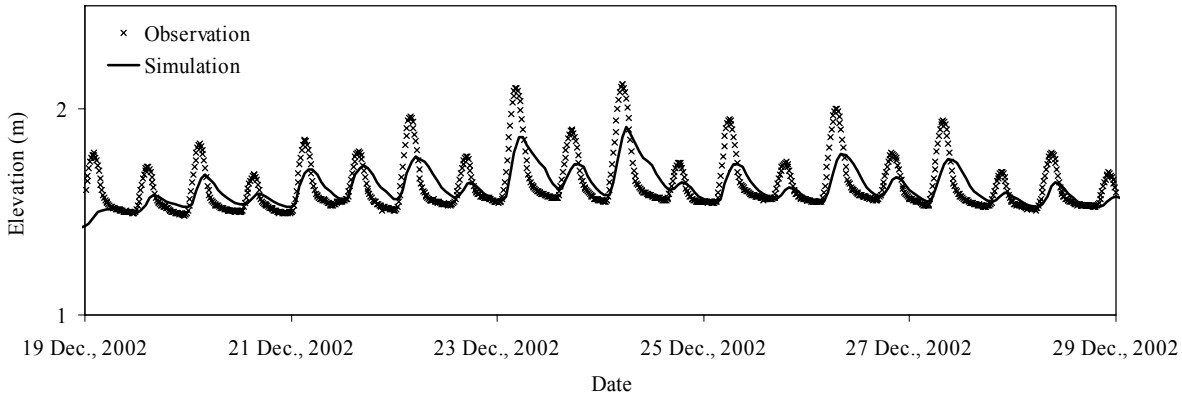

(b)

Figure 15: Comparison of observed and simulated water table fluctuations: (a) Beach; (b) Bh04

The hydrodynamic conditions were more complex beneath the beach. During the high tide state, the groundwater near the estuary flowed inland. As the groundwater away from the estuary was still flowing towards the estuary at that time, a flow convergence zone was formed in the aquifer (Figure 16a). As the tide ebbed, the water near the Mid-estuary bore flowed downward towards the estuary. The groundwater away from the estuary also flowed towards the estuary but upwards as the water above the beach (in the artificial highly permeable layer discussed above) retreated more quickly than in other areas, so inducing significant groundwater flow through it. The tidal fluctuation in the simulation produced a clockwise circulation zone near the seepage face (Figure 16b), as previously reported (Ataie-Ashtiani et al., 1999a, 2002; Mango et al, 2004). Here, we observe another anti-clockwise circulation zone (Figure 16c) under the mildly sloping beach. This zone gradually disappeared as the tide rose and the convergence zone formed. This anti-clockwise circulation zone is due to the coupled effects of tidal fluctuation, salt-water intrusion, and the small, variable beach slopes for this particular coastal aquifer. To our knowledge, this phenomenon has not been reported previously and further research both numerically and in the field is required to study it in detail.

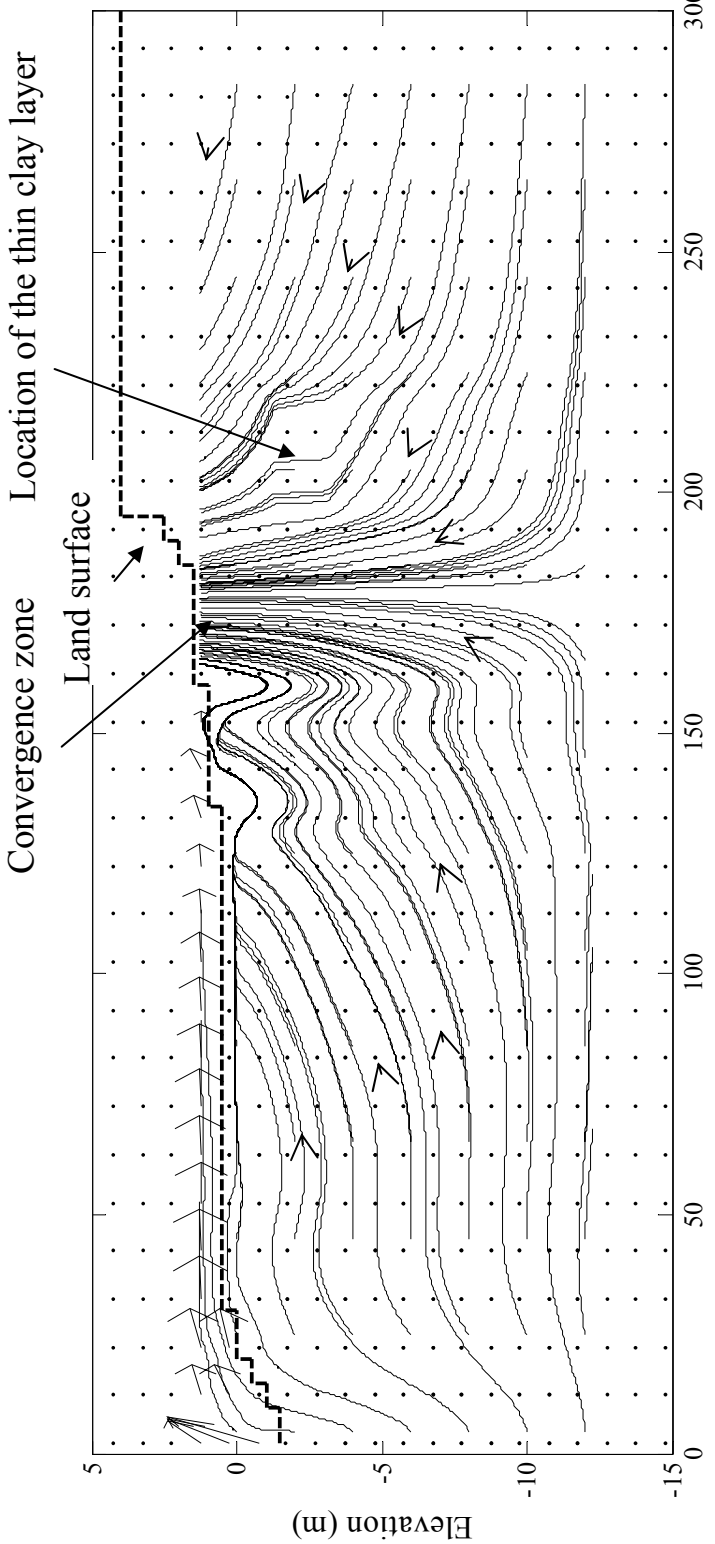

Figure 16(a): Flow field and flow lines from the simulation of the Ardeer site: (a) typical high tide state; (b) typical low tide state; and (c) the enlarged anti-clockwise circulation zone. (--- shows the morphology of the beach and aquifer)

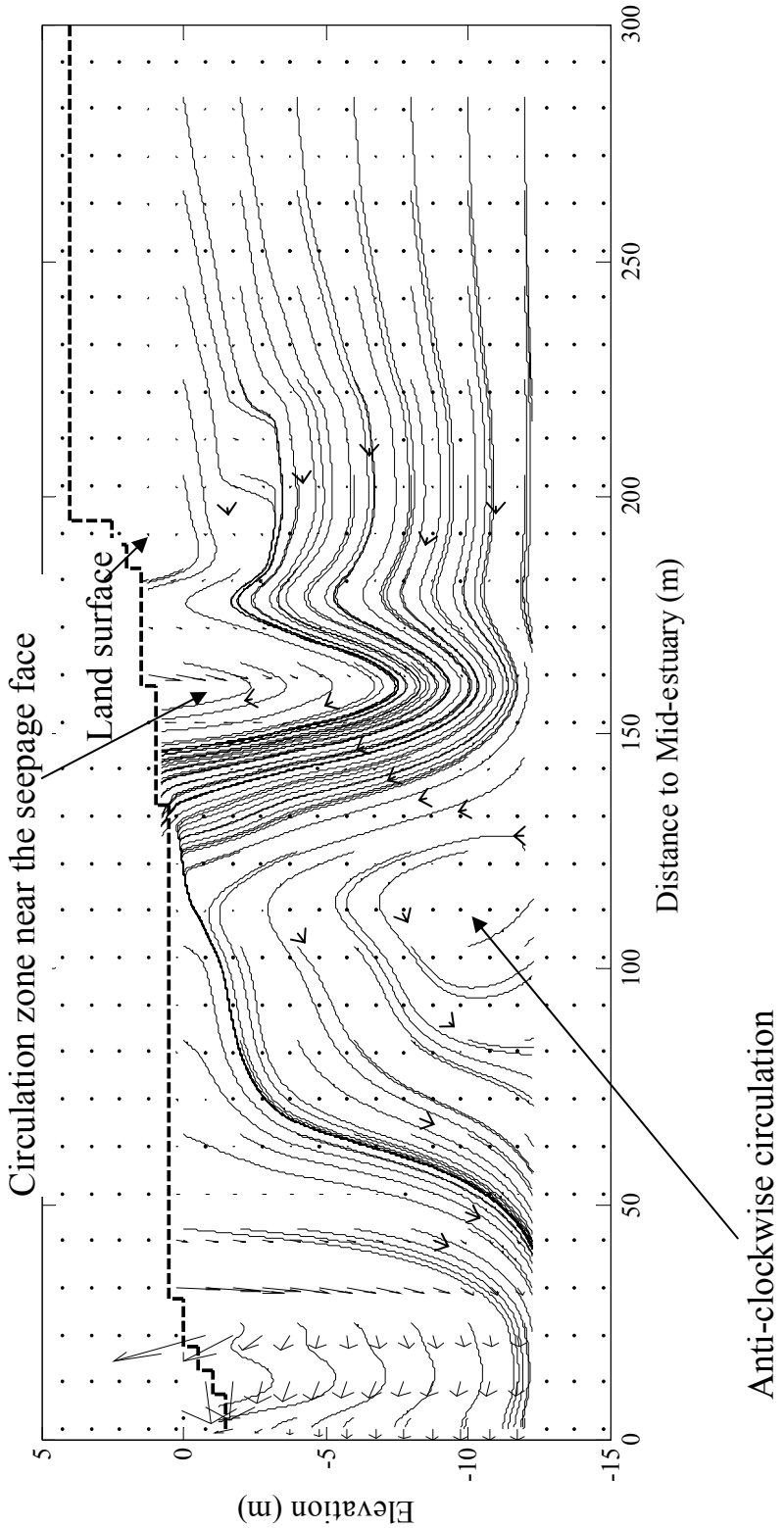

Figure 16(b): Flow field and flow lines from the simulation of the Ardeer site: (a) typical high tide state; (b) typical low tide state; and (c) the enlarged anti-clockwise circulation zone. (--- shows the morphology of the beach and aquifer)

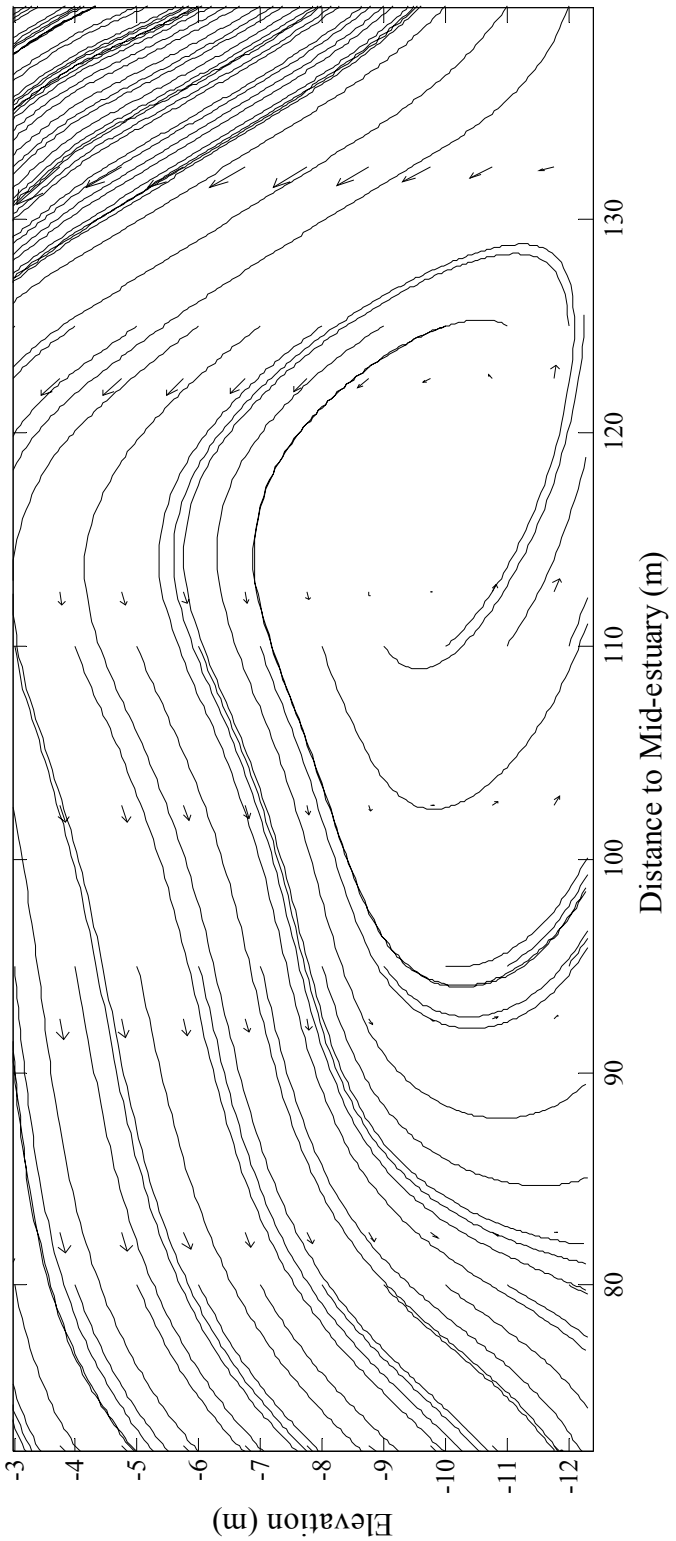

(c)

Figure 16(c): Flow field and flow lines from the simulation of the Ardeer site: (a) typical high tide state; (b) typical low tide state; and (c) the enlarged anti-clockwise circulation zone. (--- shows the morphology of the beach and aquifer)

4.2.3. Salt-water intrusion and contaminant transport

The simulated salt-water intrusion and contaminant transport are difficult to compare with field observations. For salt-water intrusion, no salinity data were collected in cross-section I-I and the salinity data from the nearby cross-section II-II require more field work for interpretation as it is thought likely that the detected salinity is due to salt-water intrusion or to contaminant migration from the landfill, the latter process having been ongoing for decades. For contaminant transport, no chemical reactions were considered as this study was aimed at investigating physical controls on conservative chemical transport in this tidally influenced aquifer.

The simulated salt-water intrusion to the aquifer is shown in Figure 17. It shows that the intrusion occurred in two ways: one is the advancement of the salt wedge at the bottom of the aquifer resulting from the density difference between salt water and fresh water. The other was the infiltration of salt water through the beach. From the 1% and 10% concentration contours, it is clear that a large mixing zone was formed underneath the beach surface. Field data showed a salinisation zone in the bottom of the aquifer near MLS01 (about 280 m away from the Mid-estuary bore), which was not reproduced by the simulation.

As might be expected, the simulation also shows that the movement of the salt wedge was small between high and low tide state (except near the beach surface), indicating that the approximation of a stationary wedge at the aquifer base will be reasonable under many circumstances.

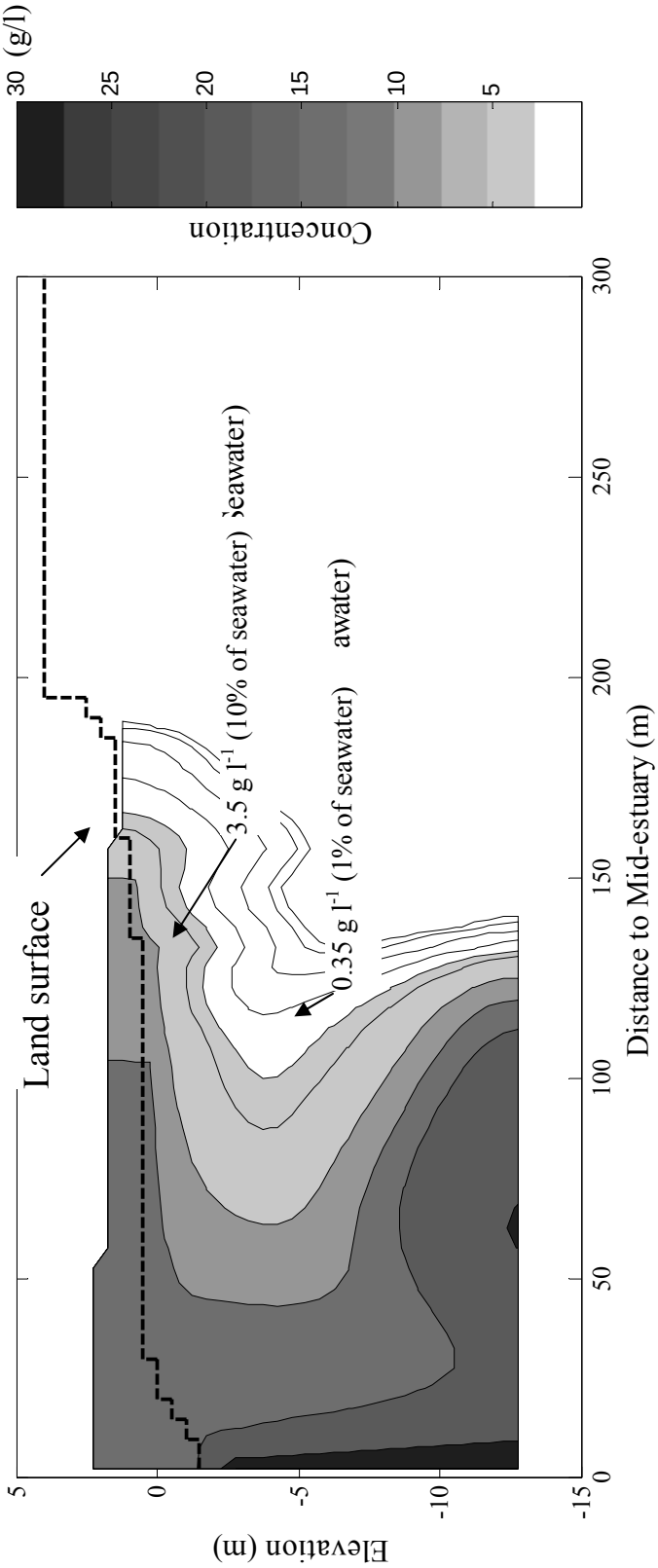

Figure 17(a): Salt-water intrusion from the simulation of the Ardeer site: (a) typical high tide result; (b) typical low tide result.

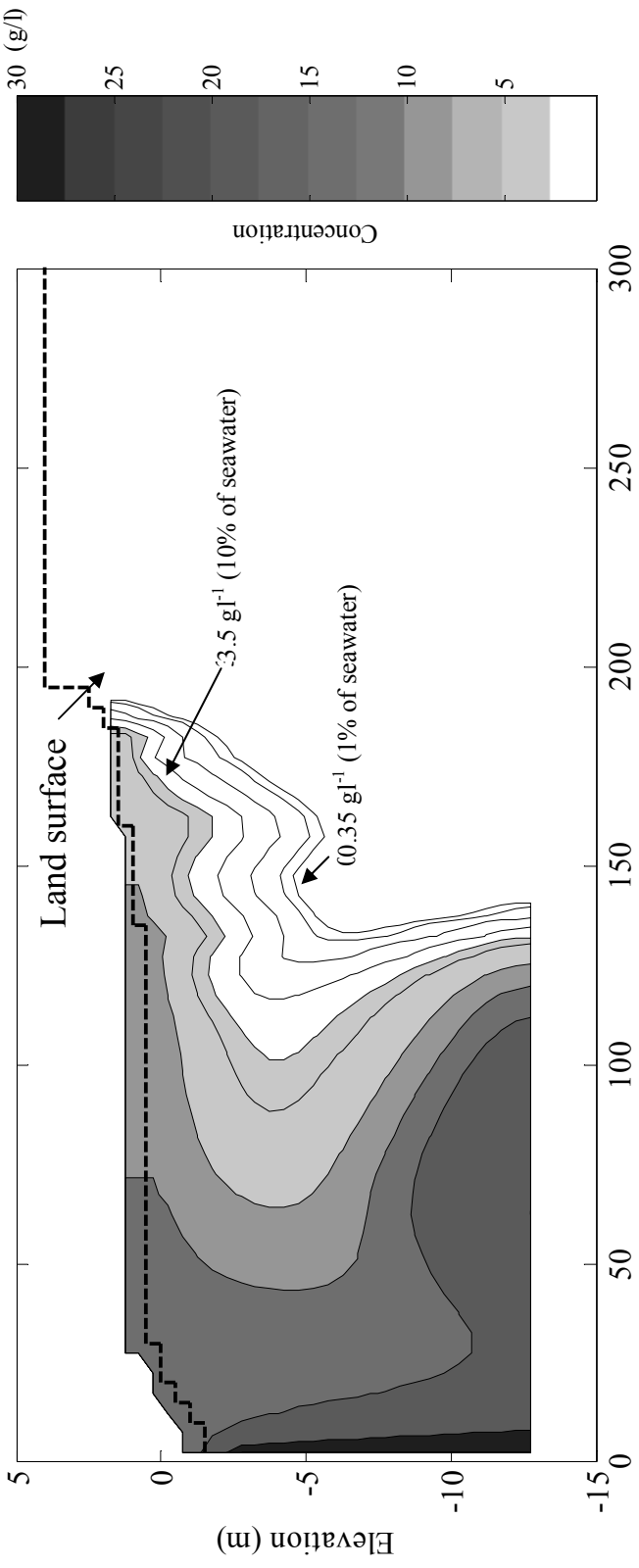

Figure 17(b): Salt-water intrusion from the simulation of the Ardeer site: (a) typical high tide result; (b) typical low tide result.

Figure 18 shows contaminant migration. After 5 years, the 10% concentration contour was located 50 m away from the Mid-estuary bore. The front of the contour inclined downwards, possibly a result of the complex hydrodynamics generated under the mildly sloping beach. Again, the concentration contours differed little between the high and low tide conditions, showing little intra-tidal response of the contaminant concentrations.

4.3. Sloping effects – comparison between two simulations

In regional simulation models and in analytical approximations, the aquifer/estuary boundary is often taken as being vertical. Previous research suggests that beach slope is significant and simplifying the problem by considering a vertical beach face may cause errors (e.g., Ataie-Ashtiani et al. 2001). In order to ascertain quantitatively the tidal effects on coastal groundwater flow and transport for different beach slopes, a comparison simulation was performed for the extreme (and artificial) case of a vertical beach. The boundary water table fluctuations, salt concentrations and the regional hydraulic properties are similar for these two cases. The difference is that the elevation of land surface is fixed at 2.5 m for the vertical beach to prevent the estuary water flowing on to the land surface.

Figure 19 shows the simulated flow lines from the vertical beach simulation. The hydrodynamics are simpler than those for the mildly sloping beach. However, there are still some characteristics that differ from the case where tidal fluctuations are ignored. The simulations show that a reverse flow zone is formed intermittently in the bottom part of the estuary. A permanent reverse flow zone would occur under the beach in the absence of tidal fluctuations as a result of density-dependent flow (Henry, 1964). With the tidal influence, this reverse-flow zone will advance into the aquifer during the rising tide, leading to a vertical convergence zone as seen for the mildly sloping beach. In the low tide state, the reverse zone disappeared as all the groundwater flow was then towards the estuary. In contrast to the results of the mild beach slope simulation, no circulation zone appeared in the vertical beach case.

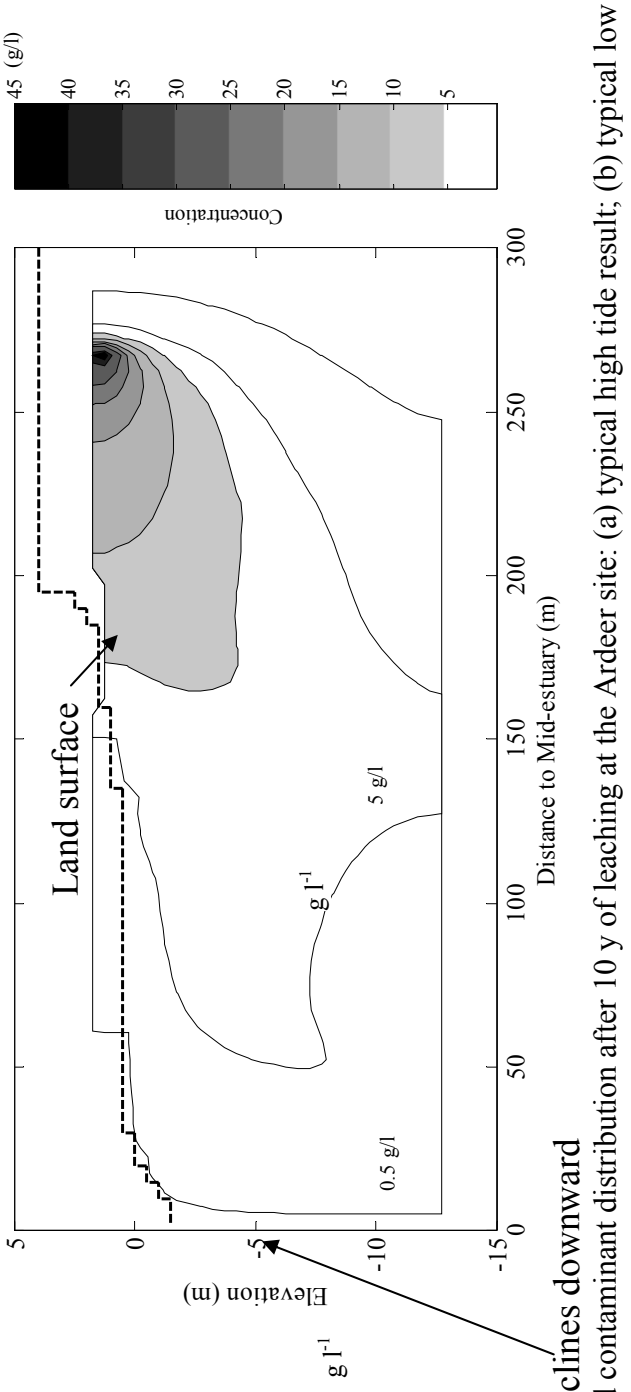

Figure 18(a): Simulated contaminant distribution after 10 y of leaching at the Ardeer site: (a) typical high tide result; (b) typical low tide result.

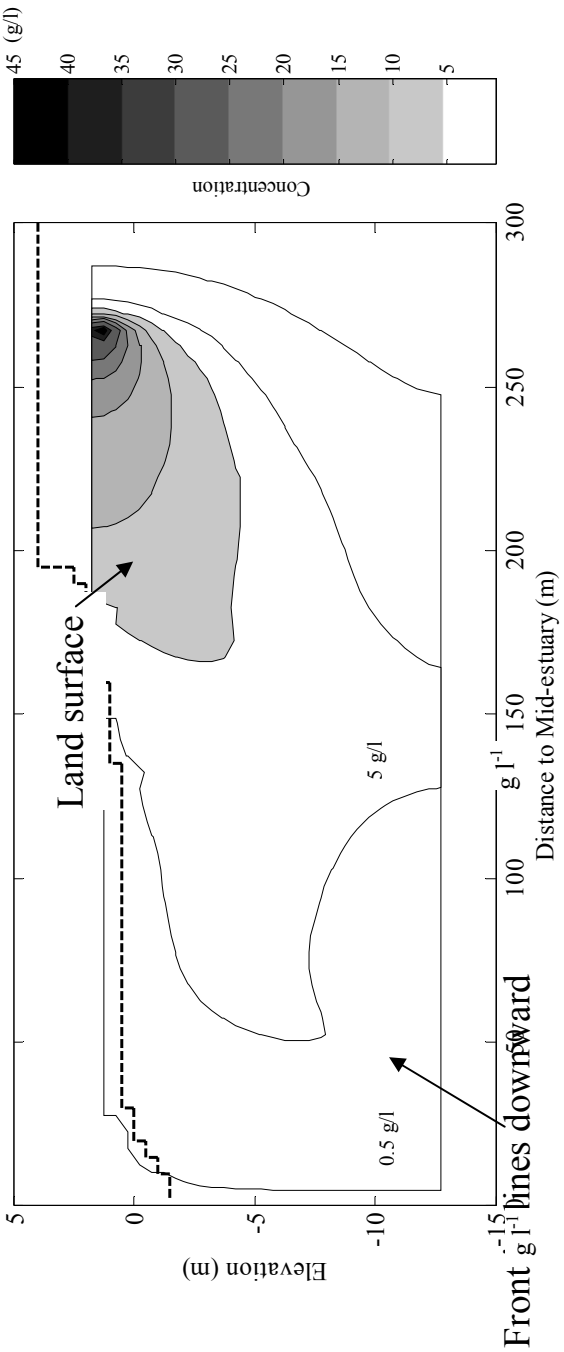

(b)

Figure 18(b): Simulated contaminant distribution after 10 y of leaching at the Ardeer site: (a) typical high tide result; (b) typical low tide result.

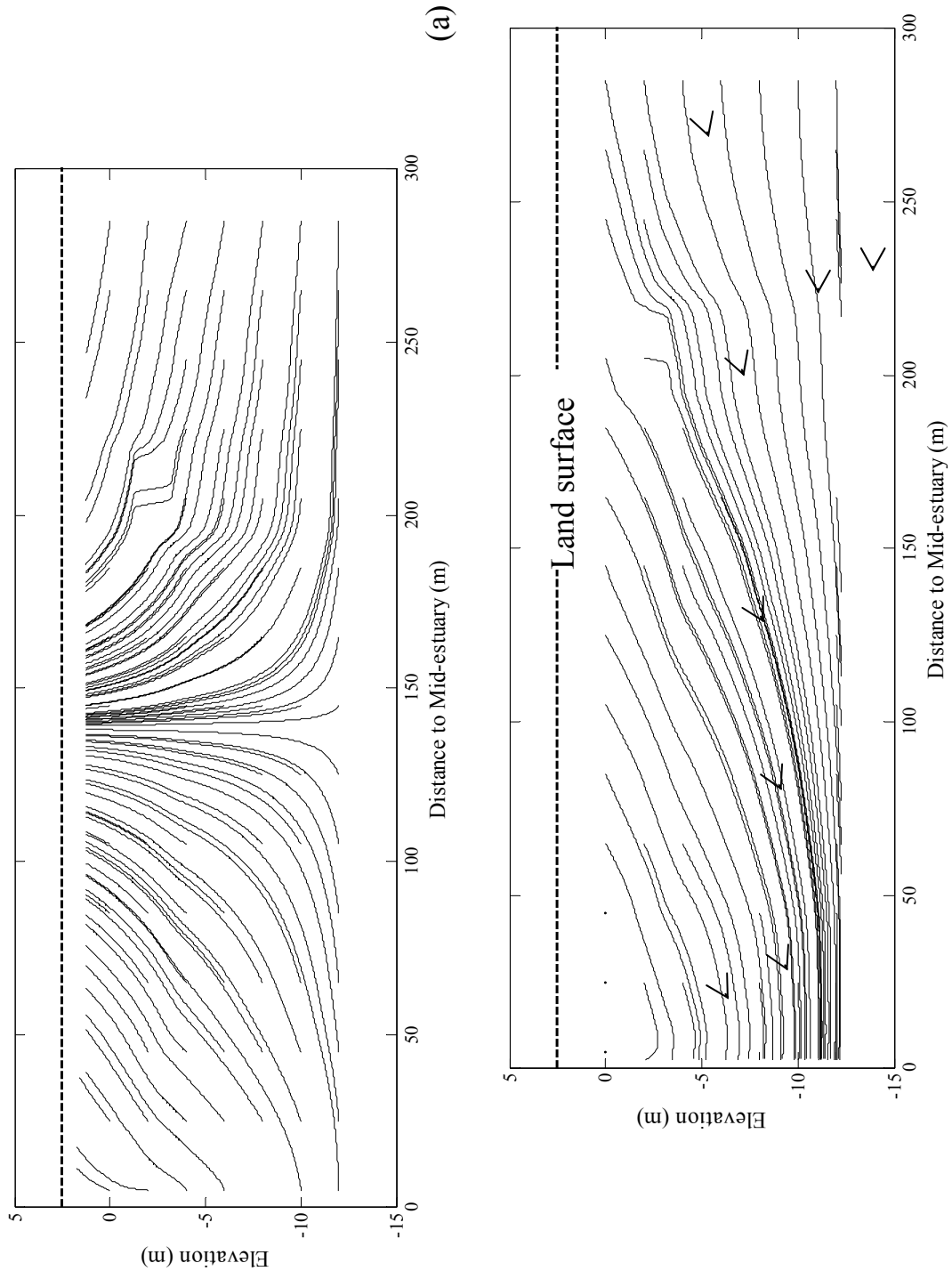

Figure 19: Flow field and flow lines within an aquifer with a vertical beach at the Mid-estuary bore: (a) typical high tide result; (b) typical low tide result.

Figure 20 shows a comparison of water table fluctuations at the Beach bore for the sloping and vertical beaches. It shows that the asymmetric character is much more apparent in the simulation with the sloping beach than that for the vertical beach, indicating that simplification of the mildly sloping beach to a vertical beach will cause errors in predicting the behaviour of tide-induced water table fluctuations.

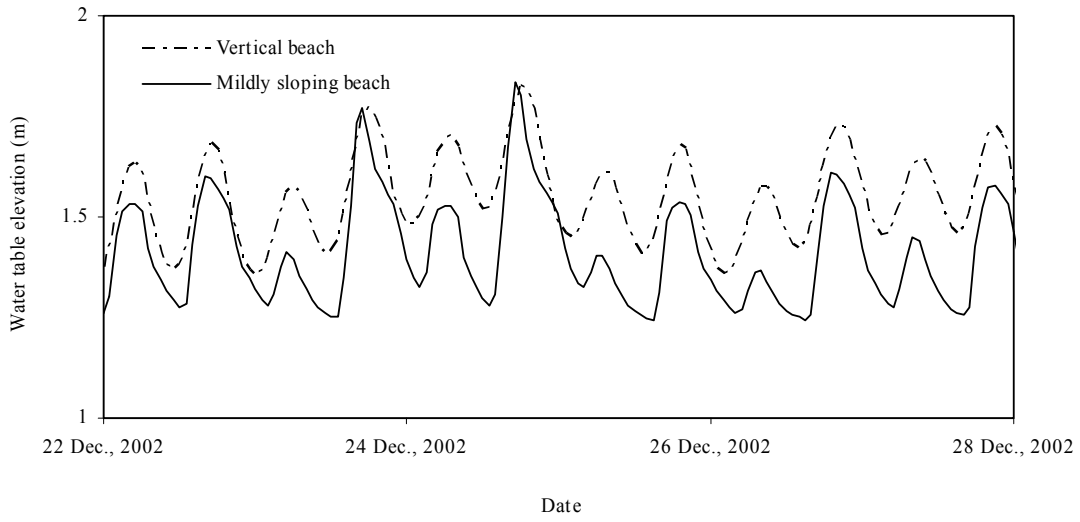

Figure 20: Comparison of the simulated water table in the Beach bore for the mildly sloping beach and the vertical beach.

The simulated salt-water intrusion for a vertical beach is shown in Figure 20. It is clear that the vertical beach simulation results exhibit much reduced salt-water intrusion in the upper part of the aquifer, as expected. Comparison of Figs. 16 and 20 indicates that the overland flow occurring on a sloping beach promotes intrusion as not only is a large area of salt-water infiltration formed under the beach surface but also the advancement of the salt wedge at the bottom of the aquifer greatly increased. This result is in agreement with that of Chen and Hsu (2004) who concluded that seawater intrusion increases with the slope of the beach. It also agrees with Ataie-Ashtiani et al. (1999a) who found that a flat beach slope intensifies the changes in the configuration of concentration contours caused by the tidal activity.

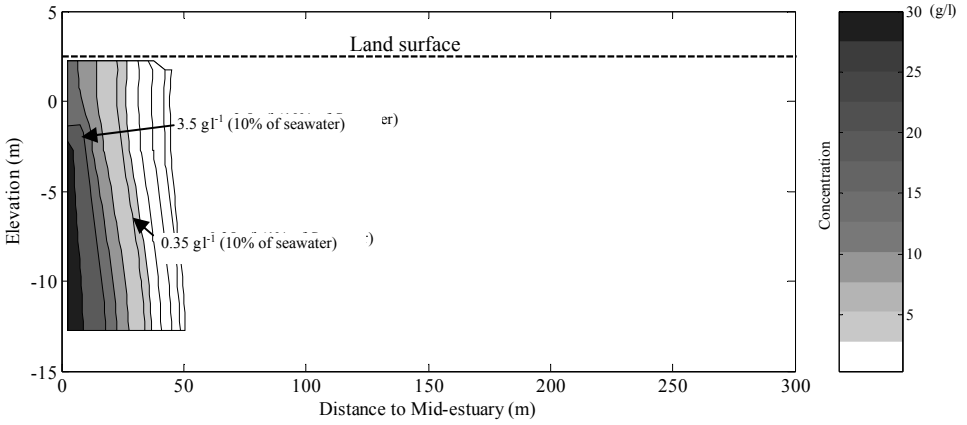

(a)

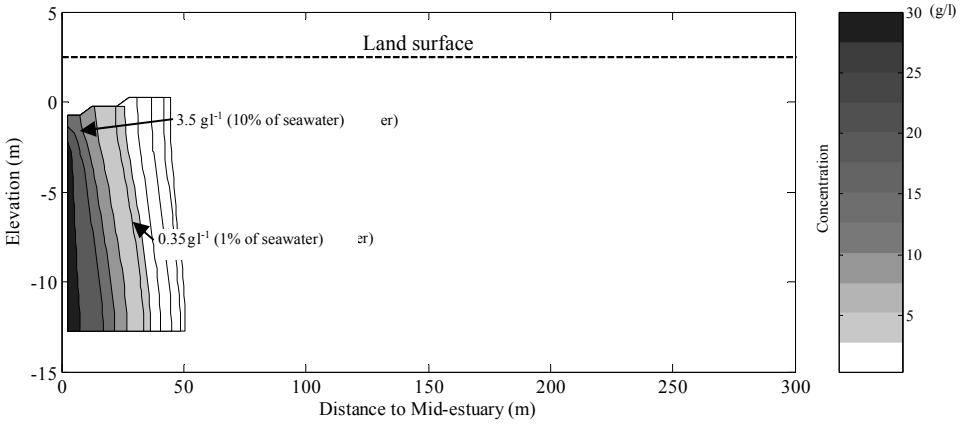

(b)

Figure 21: Salt-water intrusion with a vertical beach: (a) typical high tide result; (b) typical low tide result.

From field observations and analysis, Ullman et al. (2003) suggested that the beach face can serve as traps and reservoirs of estuarine solutes, indicating that the beach slope influences the contaminant transport to the estuary. Figure 21 shows the vertical beach simulation of the contaminant plume after 10 y of travel time. The 10% concentration contour nearly reached the estuary in this case, while it was still 50 m away from the estuary in the mildly sloping beach simulation (Figure 22). The contaminant is more widely spread in the aquifer with a vertical beach than occurs for a mildly sloping beach. Possibly the mildly sloping beach has inhibited the plume transport, or the plume under the beach is greatly diluted for this case. To further investigate this result, we compared the net contaminant output towards the estuary from the aquifer by calculating the horizontal flux across the vertical line 180 m landward of the Mid-estuary bore (see the dotted line shown in Figure 13). As shown in Figure 22a, the fluxes are mostly negative (off-shore) in both cases, indicating that the contaminant transport is towards the estuary. The fluxes fluctuate with the

tide although a phase lag is apparent. This fluctuation is more distinct for the mildly sloping beach; however the averaged outputs do not vary much for the two cases, with the flux in the mild slope case 8% larger than that for the vertical beach.

After the contaminant entered the area under the beach, the continuing horizontal output at 30 m from the Mid-estuary bore is shown in Figure 22b (see the dashed line shown in Figure 13). In contrast to Figure 22a, the flux in the vertical beach case shows a more prominent influence due to the tidal fluctuation. The output from the vertical beach is about 5% more than that from the mildly sloping beach. This is because more salt-water intrusion occurs under the mildly sloping beach and the reverse flow reduces the horizontal contaminant output towards the estuary.

As it is possible for the contaminant to move vertically to the beach surface under the mildly sloping beach, we calculated the upward/downward flux rate along the beach at depths of 0.5 - 1 m below the beach surface (see the dash-dot line shown in Figure 13) in the typical high and low tide states, and the average effect over 1 d, as shown in Figure 22c. The vertical flux mainly occurs in the area between 150 m to 180 m from the Mid-estuary bore, showing large variations both temporally and spatially. At the high tide stage, the flux is downward into the aquifer between 150 m to 165 m, and upward to the beach between 165 m to 180 m. At the low tide stage, the flux direction is more complex but mostly upward between 150 m to 165 m, and downward between 165 m to 180 m. This is consistent with the hydrodynamics shown previously for the mildly sloping beach (Figure 15). The averaged effect for a 1-d period shows discharge to the beach between 150 m to 165 m. It indicates that although the contaminant contour shows little intra-tidal response to tidal fluctuations, it is still possible that the complex flux pattern generated under the mildly sloping beach brings solute to the beach surface.

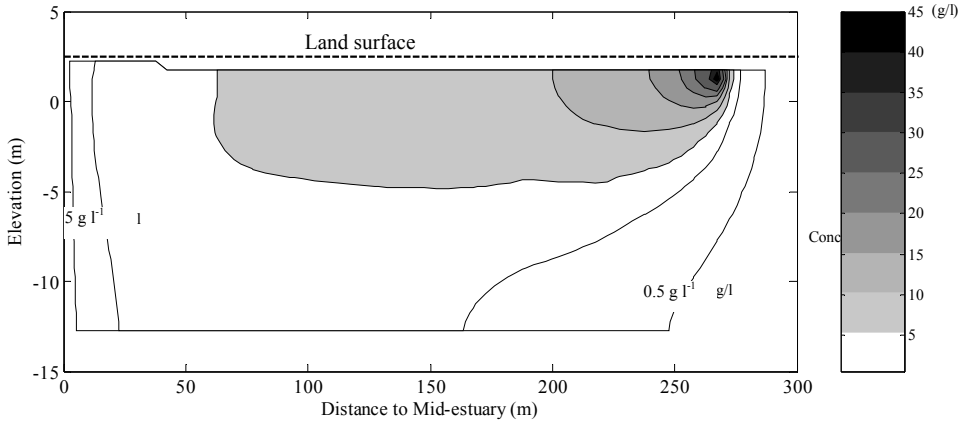

(a)

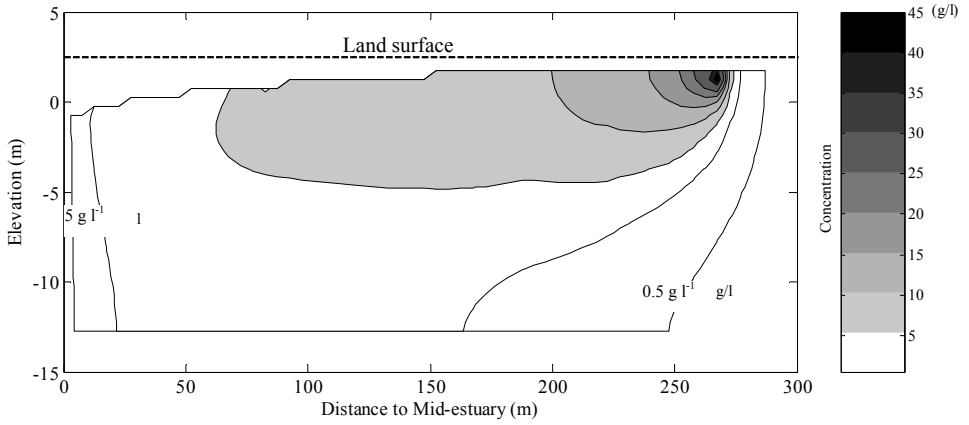

(b)

Figure 22: Contaminant distribution after 10 y transport: (a) typical high tide result; (b) typical low tide result.

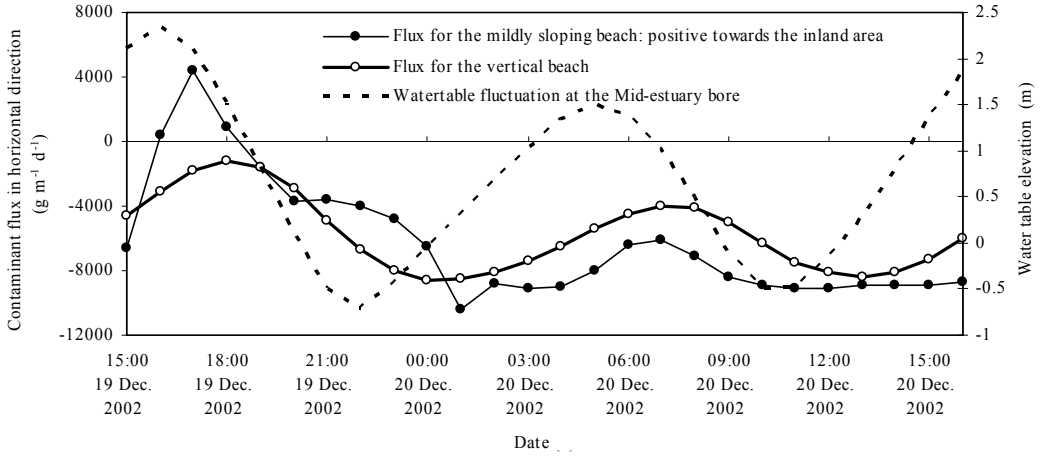

(a)

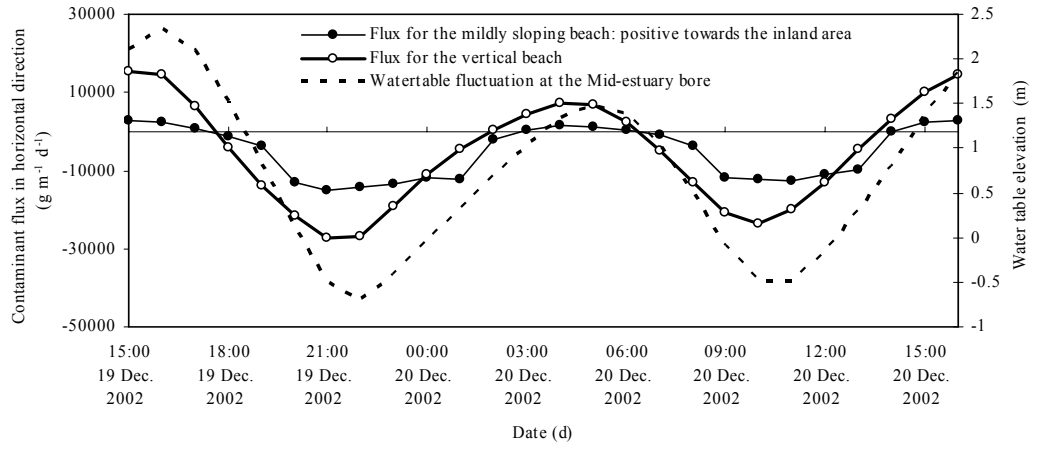

(b)

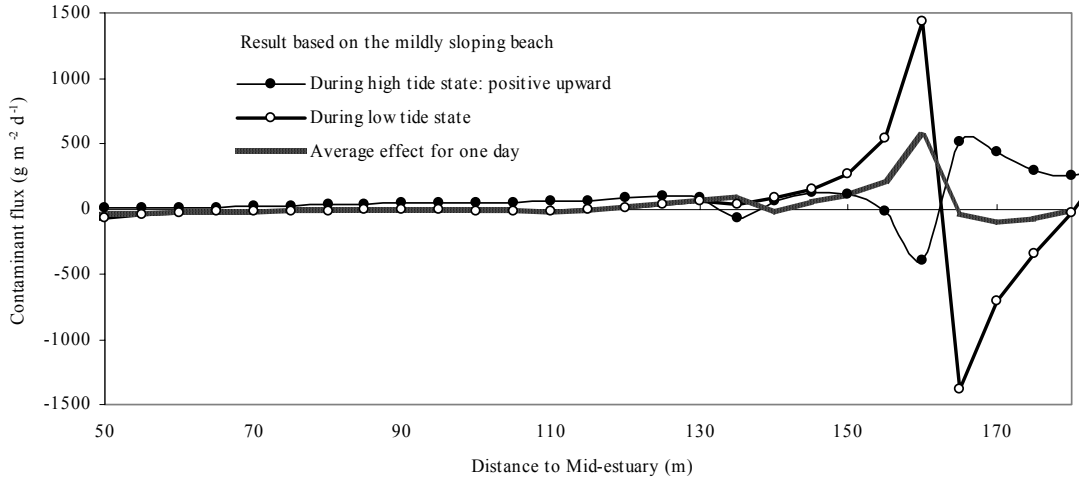

(c)

Figure 23. Simulation results of contaminant flux: (a) the horizontal flux across the vertical line 180 m from the Mid-estuary bore and corresponding tidal fluctuations; (b) the horizontal flux across the vertical line 30 m from the Mid-estuary bore and corresponding tidal fluctuations; and (c) the vertical flux below the beach over the horizontal distance between 50 m to 180 m from the Mid-estuary bore.

5. Concluding Remarks

Both the field monitoring and simulations have shown that groundwater dynamics, salt-water intrusion and chemical transport in a coastal aquifer are influenced by tidal fluctuations and that this influence is intensified when the aquifer is adjacent to a low-relief estuary.

The tide-induced groundwater table fluctuations will have exponentially decreasing amplitude and linearly increasing phase lag with increasing distance from the estuary, as revealed by the FFT analysis. For this mildly sloping beach, the water table fluctuations were profoundly asymmetric, having a sharp rise and slow decline, a feature captured by numerical solutions.

Small beach slopes will enhance the tidal effects on coastal groundwater dynamics (flow and solute transport). On the rising tide, the reverse flow zone typical for seawater intrusion moved inland, expanded and formed a vertical convergence zone. On the ebb tide, an anti-clockwise circulation zone appeared under the sloping beach. Both the density difference and the tidal propagation led to salt-water intrusion into the bottom part of the aquifer and through the beach surface, forming a large mixing zone that would not exist at a vertical beach. In relation to the contaminant migration towards the estuary, the tidal effect will lead to fluctuations of contaminant fluxes to the estuary. For a mildly sloping beach, tidal effect also generates strong vertical contaminant flux near the vicinity of the shoreline. This vertical mass exchange along the beach surface might result in contamination in the lower-relief estuary and could possibly put the ecosystem at risk in this region.

Our numerical study showed that the low-relief estuary will result in complex flow patterns when accompanied with the tidal fluctuations. The numerical predictions suggest that monitoring should consider beach morphology, changes in hydraulic properties, as well as methods capable of quantifying the hydrodynamics and salinity underneath the beach. In particular, we have identified the influence of density difference and tidal fluctuations on flow patterns and accompanying solute transport when the aquifer is adjacent to the low-relief estuary, e.g., a circulation zone was found under the beach, and a tide-induced upward discharge was noticed near the bank. Notwithstanding the complex flow patterns beneath the beach, simulations showed that there is no obvious movement of the salt wedge (either at the aquifer base or beneath the beach face) over a tidal cycle. Likewise, for the contamination

plume there are no distinct intra-tidal variations of the concentration, at least for the conditions of the Ardeer site.

Acknowledgements

The authors thank C. Langevin for kindly providing help in using SEAWAT-2000 and B.S. Miller for providing material about Ardeer site. Significant field support was provided by P. Winship. The research was supported by the Leverhulme Trust (grant no. F/00 158/J).

References

Ataie-Ashtiani, B., Volker, R.E., Lockington, D.A., 1999a. Tidal effects on sea water intrusion in unconfined aquifers. Journal of Hydrology 216, 17-31.

Ataie-Ashtiani, B., Volker, R.E., Lockington, D.A., 1999b. Numerical and experimental study of seepage in unconfined aquifers with a periodic boundary condition. Journal of Hydrology 222, 165-184

Ataie-Ashtiani, B., Volker, R.E., Lockington, D.A., 2001. Tidal effects on groundwater dynamics in unconfined aquifers. Hydrological Processes 15, 655-669.

Ataie-Ashtiani, B., Volker, R.E., Lockington, D.A., 2002. Contaminant transport in the aquifers influenced by tide, Australian civil Engineering Transactions, Institution of Engineers, Australia, CE43, pp. 1-11.

Barry, D.A., Barry S.J., Parlange J.-Y., 1996. Capillarity correction to periodic solutions of the shallow flow approximation, In Mixing Processes in Estuaries and Coastal Seas, C.B. Pattiaratchi (editor), Coastal and Estuarine Studies, Volume 50, American Geophysical Union, Washington, DC, pp. 496-510.

Bear, J., Cheng, A.H.-D., Sorek, S., Ouazar, D., Herrera, I., 1999. Seawater Intrusion in Coastal Aquifers – Concepts, Methods and Practices. Kluwer Academic Publishers. Dordrecht.

Buddemeier, R.W., 1996. Groundwater flux to the ocean: Definitions, data, applications, uncertainties. In Buddemeier, R.W. (Ed.), Groundwater Discharge in the Coastal Zone: Proceedings of an International Symposium. LOICZ IGBP. LOICZ/R&S/96-8, Texel, The Netherlands, pp. 16-21.

Cartwright, N., Li, L., Nielsen, P., 2004. Response of the salt–freshwater interface in a coastal aquifer to a wave-induced groundwater pulse: Field observations and modelling. Advances in Water Resources 27, 297–303.

Chen, B.F., Hsu, S.M., 2004. Numerical study of tidal effects on seawater intrusion in confined and unconfined aquifers by time-independent finite-difference method. ASCE Journal of Waterway, Port, Coastal, and Ocean Engineering 130, 191-206.

Cheng, A.H.-D., Ouazar, D. (Eds.), 2003. Coastal Aquifer Management Monitoring, Modelling, and Case Studies. Lewis Publishers, Boca Raton, Florida, USA.

Erskine, A.D., 1991. The effect of tidal fluctuation on a coastal aquifer in the UK. Ground Water 19, 556-562.

Gallagher, D.L., Dietrich, A.M., Reay, W.G., Hayes, M.C., Simmons, G.M. Jr., 1996. Ground water discharge of agricultural pesticides and nutrients to estuarine surface water. Ground Water Monitoring and Remediation 16, 118-129.

Guo, W., Langevin, C.D., 2002. User's Guide to SEAWAT: A Computer Program for Simulation of Three-Dimensional Variable-Density Ground-Water Flow. U.S. Geological Survey Techniques of Water-Resources Investigations, Book 6 USA.

Henry, H.R., 1964. Effects of dispersion on salt encroachment in coastal aquifers, sea water in coastal aquifers. US Geological Survey Water Supply Paper 1613-C, 70-84 USA.

Jeng, D.-S., Seymour, B.R., Barry, D.A., Parlange, J.-Y., D. A. Lockington, D.A., Li, L., 2005a. Steepness expansion for free surface flows in coastal aquifers. Journal of Hydrology 309, 85-92.

Jeng, D.-S., Mao, X., Enot, P., Barry, D.A., Li, L., 2005b. Spring-neap tide-induced beach water table fluctuations in a sloping coastal aquifer. Water Resources Research 41, W07026, doi:10.1029/2005WR003945.

Jiao, J.J., Tang, Z., 1999. An analytical solution of groundwater response to tidal fluctuation in a leaky confined aquifer. Water Resources Research 35, 747-751.

Kaleris, V., Lagas, G., Marczinek, S., Piotrowski, J.A., 2002. Modelling submarine groundwater discharge: an example from the western Baltic Sea. Journal of Hydrology 265, 76-99.

Langevin, C.D., Shoemaker, W.B., Guo, W., 2003. MODFLOW-2000, the U.S. Geological Survey Modular Ground-Water Model ─ Documentation of the SEAWAT-2000 Version with the Variable-Density Flow Process (VDF) and the Integrated MT3DMS Transport Process (IMT). US Geological Survey Open-File Report 03-426 Tallahassee, Florida, USA.

Li, L., Barry, D.A., Pattiaratchi, C.B., 1997. Numerical modelling of tide-induced beach water table fluctuations. Coastal Engineering 30, 105-123.

Li, L., Barry, D.A., Stagnitti, F., Parlange, J.-Y., 1999. Submarine groundwater discharge and associated chemical input to a coastal sea. Water Resources Research 35, 3253-3259.

Li, L., Barry, D.A., 2000a. Wave-induced beach groundwater flow. Advances in Water Resources 23, 325-337.

Li, L., Barry, D.A., Cunningham, C., Stagnitti, F., Parlange, J.-Y., 2000b. A two-dimensional analytical solution of groundwater responses to tidal loading in an estuary and ocean. Advances in Water Resources 23, 825-833.

Li, L., Barry, D.A., Stagnitti, F., Parlange, J.-Y., Jeng D.-S., 2000c. Beach water table fluctuations due to spring–neap tides: Moving boundary effects. Advances in Water Resources 23, 817-824.

Li, L., Barry D.A., Stagnitti, F., Parlange J.-Y. 2000d. Groundwater waves in a coastal aquifer: A new governing equation including vertical effects and capillarity. Water Resources Research. 36, 411-420.

Li, L., Barry, D.A., Pattiaratchi, C.B., Masselink, G., 2002. BeachWin: Modelling groundwater effects on swash sediment transport and beach profile changes. Environmental Modelling and Software 17, 313-320.

Mango, A.J., Schmeeckle, M.W., Furbish, D.J., 2004. Tidally induced groundwater circulation in an unconfined coastal aquifer modeled with a Hele-Shaw cell. Geology 32, 233-236.

McDonald, M.C., Harbaugh, A.W., 1998. MODFLOW, a modular three-dimensional finite difference ground water flow model. US Geological Survey, Open-file Report 83-875, USA.

Moore, W.S., 1996. Large groundwater inputs to coastal waters revealed by Ra-226 enrichments. Nature 380, 612-614.

Nielsen, P., 1990. Tidal dynamics of the water table in beaches. Water Resources Research 26, 2127-2134.

Purnalna, A., Al-Barwani, H.H., Al-Lawatia, M., 2003. Modelling dispersion of brine waste discharges from a coastal desalination plant. Desalination 155, 41-47.

Raubenheimer, B., Guza, R.T., 1999. Tidal water table fluctuations in a sandy ocean beach. Water Resources Research 35, 2313-2320.

Robinson, M.A., Gallagher, D.L., Reay, W., 1998. Field observations of tidal and seasonal variations in ground water discharge to tidal estuarine surface water. Ground Water Monitoring and Remediation 18, 83-92.

Simmons, G.M., 1992. Importance of submarine groundwater discharge and sea water cycling to material flux across sediment/water interfaces in marine environments, Marine Ecology Progress Series 84, 173-184.

Su, N., Liu, F., Anh, V., 2003. Tides as phase-modulated waves inducing periodic groundwater flow in coastal aquifers overlaying a sloping impervious base. Environmental Modelling and Software 18, 937-942.

Teo, H.T., Jeng, D.S., Seymour, B.R., Barry, D.A., Li, L., 2003. A new analytical solution for water table fluctuations in coastal aquifers with sloping beaches. Advances in Water Resources 26, 1239-1247.

Trefry, M.G., 1999. Periodic forcing in composite aquifers. Advances in Water Resources 22, 645-656.

Trefry, M.G., Bekele, E., 2004. Structural characterization of an island aquifer via tidal methods. Water Resources Research 40, W01505 10.1029/ 2003WR002003.

Uchiyama, Y., Nadaoka, K., Rolke, P., Adachi, K., and Yagi, H., 2000. Submarine groundwater discharge into the sea and associated transport in a sandy beach. Water Resources Research 36, 1467-1479.

Ullman, W.J., Chang, B., Miller, D.C., Madsen, J.A., 2003. Groundwater mixing, nutrient diagenesis, and discharges across a sandy beachface, Cape Henlopen, Delaware (USA). Estuarine, Coastal and Shelf Science 57, 539-552.

Voss, C.I., 1984. SUTRA: A finite-element simulation model for saturated-unsaturated fluid-density-dependent ground-water flow with energy transport or chemically-reactive single-species solute transport. US Geological Survey Water Resources Investigation Report 84-4369, pp. 409, USA.

Weiskel, P.K., Howes, B.L., 1992. Differential transport of sewage derived nitrogen and phosphorous through a coastal watershed. Environmental Science and Technology 26, 352-360.

Zheng, C., Wang, P.P., 1999. MT3DMS, A Modular Three-Dimensional Multi-Species Transport Model for Simulation of Advection, Dispersion and Chemical Reactions of Contaminants in Groundwater Systems; Documentation and User's Guide. US Army Engineer Research and Development Centre Contract Report SERDP-99-1, Vicksburg, MS, pp. 202, USA.

Appendix: Derivation of analytical solutions

In this appendix, we provide the detailed derivation of analytical solution, which is presented in Section 3.

To simplify the mathematical procedure, we introduce the following non-dimensional variables [Teo et al., 2003]:

$$X_1 = \frac{x}{L}, \quad H = \frac{h}{D}, \quad \Phi = \frac{\phi}{D}, \quad \text{and} \quad T{=}\omega_1 t, \tag{7}$$

where $L = \sqrt{2KD/n_e\omega_1}$ is the linear decay length.

We further employ a co-ordinate transformation [Li et al., 2000c],

$$X = X_1 - \alpha\varepsilon \cot(\beta) \left[\cos(T + \delta_1) + \lambda \cos(\omega T + \delta_2)\right], \tag{8}$$

where $\varepsilon = \sqrt{n_e\omega_1 D/2K}$ is the shallow water parameter, $\alpha = A_1/D$ is the amplitude parameter, $\lambda = A_2/A_1$ is the ratio of amplitude of two tidal components, $\omega = \omega_2/\omega_1$ is the ratio of frequencies of two tidal components, and δ_1 and δ_2 are the phase of each component.

Using the shallow water parameter (ε), the non-dimensional water table level (H) and potential head (Φ) can be expanded as:

$$H = H_0 + \varepsilon H_1 + \varepsilon^2 H_2 + \cdots, \quad \text{and} \quad \Phi = \Phi_0 + \varepsilon\Phi_1 + \varepsilon^2\Phi_2 + \cdots, \tag{9}$$

Substituting (9) into the governing equations and boundary conditions [i.e., equation (1) and (2a)-(2b), (2e) in the text], the kinematic boundary condition [(2c) in the tex] can be sorted in terms of the shallow water parameter as

$$O(1) \quad : \quad 2H_{0T} = \left(H_0 H_{0X}\right)_X, \tag{10a}$$

$$O(\varepsilon) \quad : \quad 2\left\{H_{1T} + \alpha \cot\beta \left[\sin(T + \delta_1) + \lambda\omega \sin(\omega T + \delta_2)\right] H_{0X}\right\} = \left(H_0 H_1\right)_{XX}, \tag{10b}$$

$$O(\varepsilon^2) \quad : \quad 2\left\{H_{2T} + \alpha \cot\beta \left[\sin(T + \delta_1) + \lambda\omega \sin(\omega T + \delta_2)\right] H_{1X}\right\} = \frac{1}{2}\left(H_1^2\right)_{XX} + \left(H_0 H_2\right)_{XX} + \frac{1}{3}\left(H_0^3 H_{0XX}\right)_{XX}. \tag{10c}$$

Since the above equations are non-linear, the amplitude parameter ($\alpha = A_1/D$) is used to expand the various equations in order to solve them approximately, that is,

$$H_0 = 1 + \alpha H_{01} + \alpha^2 H_{02} + \cdots, \text{ and } H_n = \alpha H_{n1} + \alpha^2 H_{n2} + \cdots \quad (n \geq 1). \tag{11}$$

Then, (10a)-(10c) can be further sorted in terms of the amplitude parameter (α) as

$$O(\alpha) \quad : \qquad 2H_{01T} = H_{01XX}, \tag{12a}$$

$$O(\alpha^2) \quad : \qquad 2H_{02T} = H_{02XX} + \frac{1}{2}\left(H_{01}^2\right)_{XX}, \tag{12b}$$

$$O(\varepsilon\alpha) \quad : \qquad 2H_{11T} = H_{11XX}, \tag{12c}$$

$$O(\varepsilon\alpha^2) \quad : \qquad 2H_{12T} = H_{12XX} - 2\cot\beta\left[\sin(T+\delta_1) + \lambda\omega\sin(\omega T + \delta_2)\right] H_{01X}, \tag{12d}$$

$$O(\varepsilon^2\alpha) \quad : \qquad 2H_{21T} = H_{21XX} + \frac{1}{3}H_{01XXXX}. \tag{12e}$$

The above equations (12a)-(12e) are solved with the following boundary conditions:

$$H_{01}(0,T) = \cos(T+\delta_1) + \lambda\cos(\omega T + \delta_2), \tag{13a}$$

$$H_{02}(0,T) = H_{11}(0,T) = H_{12}(0,T) = H_{21}(0,T) = 0, \tag{13b}$$

$$H_{01X}(\infty,T) = H_{02X}(\infty,T) = H_{11X}(\infty,T) = H_{12X}(\infty,T) = H_{21X}(\infty,T) = 0 \tag{13c}$$

The solution of water table elevation in the above boundary value problem is summarized here:

$$H = 1 + \left(\alpha H_{01} + \alpha^2 H_{02}\right) + \varepsilon\left(\alpha H_{11} + \alpha^2 H_{12}\right) + \varepsilon^2\alpha H_{21}, \tag{14}$$

which is the non-dimensional form of equation (3) in the text. The functions on the righ-hand-side are given by

$$H_{01} = e^{-X}\cos(\theta_1+\delta_1) + \lambda e^{-\sqrt{\omega}X}\cos(\eta_1+\delta_2), \tag{15}$$

$$\begin{aligned} H_{02} &= \frac{1}{4}\left(1-e^{-2X}\right) + \frac{\lambda^2}{4}\left(1-e^{-2\sqrt{\omega}X}\right) \\ &+\frac{1}{2}\left[e^{-\sqrt{2}X}\cos(\theta_2+2\delta_1) + \lambda e^{-2X}\cos 2(\theta_1+\delta_1)\right] \\ &+\frac{\lambda^2}{2}\left[e^{-\sqrt{2\omega}X}\cos(\eta_2+2\delta_1) - e^{-2\sqrt{\omega}X}\cos 2(\eta_1+\delta_2)\right] \\ &+\frac{\lambda\left(1+\sqrt{\omega}\right)^2}{4\sqrt{\omega}}\left[e^{-\sqrt{1+\omega}X}\cos(\eta_3+\delta_1+\delta_2) - e^{-(1+\sqrt{\omega})X}\cos(1+\omega)T\right] \\ &+\frac{\lambda}{2}\left[e^{-(1+\sqrt{\omega})X}\cos(\theta_1-\eta_1+\delta_1-\delta_2) - e^{-\sqrt{1+\omega}X}\cos(\eta_4+\delta_1-\delta_2)\right] \\ &+\frac{\lambda(1-\omega)}{4\sqrt{\omega}}\left[e^{-(1+\sqrt{\omega})X}\sin(\theta_1-\eta_1+\delta_1-\delta_2) - e^{-\sqrt{1-\omega}X}\cos(\eta_4+\delta_1-\delta_2)\right], \end{aligned} \tag{16}$$

$$H_{11} = 0, \tag{17}$$

$$\begin{aligned} H_{12} &= \frac{1}{\sqrt{2}}\cot\beta\left\{\frac{1}{\sqrt{2}} - e^{-X}\cos(X-\frac{\pi}{4}) + \lambda^2\sqrt{\omega}\left[\frac{1}{\sqrt{2}} - e^{-\sqrt{\omega}X}\cos(\sqrt{\omega}X-\frac{\pi}{4})\right]\right. \\ &+\left[e^{-\sqrt{2}X}\cos(\theta_2+2\delta_2+\frac{\pi}{4}) - e^{-X}\cos(\theta_3+2\delta_1+\frac{\pi}{4})\right] \\ &+\frac{\lambda^2}{2}\left[e^{-\sqrt{2\omega}X}\cos(\eta_2+2\delta_2) - e^{-2\sqrt{\omega}X}\cos 2(\eta_1+\delta_2)\right] \\ &+\lambda\sqrt{\omega}\left[e^{-\sqrt{1+\omega}X} - e^{-\sqrt{\omega}X}\right]\cos(\eta_3+\delta_1+\delta_2+\frac{\pi}{4}) \\ &+\lambda\sqrt{\omega}\left[e^{-\sqrt{\omega}X}\cos(T-\eta_1+\delta_1-\delta_2-\frac{\pi}{4}) - e^{-\sqrt{1-\omega}X}\cos(\eta_4+\delta_1-\delta_2-\frac{\pi}{4})\right] \\ &+\lambda\left[e^{-\sqrt{1+\omega}X}\cos(\eta_3+\delta_1+\delta_2+\frac{\pi}{4}) - e^{-X}\cos(\theta_1+\omega T+\delta_1+\delta_2+\frac{\pi}{4})\right] \\ &+\lambda\left[e^{-\sqrt{1-\omega}X}\cos(\eta_4+\delta_1-\delta_2+\frac{\pi}{4}) - e^{-X}\cos(\theta_1+\omega T+\delta_1-\delta_2+\frac{\pi}{4})\right] \\ &\left.+\frac{\lambda\sqrt{\omega}}{\sqrt{2}}\left[e^{-\sqrt{2\omega}X}\cos(\eta_2+2\delta_2+\frac{\pi}{4}) - e^{-\sqrt{\omega}X}\cos(\theta_1+\omega T+2\delta_2+\frac{\pi}{4})\right]\right\}, \end{aligned} \tag{18}$$

$$H_{21} = -\frac{\sqrt{2}}{3}\left[Xe^{-X}\cos(\theta_1+\delta_1+\frac{\pi}{4}) + \frac{\lambda\omega^2}{\sqrt{\omega}}e^{-\sqrt{\omega}X}\cos\left(\eta_1+\delta_2-\frac{\pi}{4}\right)\right], \tag{19}$$

where $\theta_1 = T - X$, $\theta_2 = 2T - \sqrt{2}X$, $\theta_3 = 2T - X$, $\eta_1 = \omega T - \sqrt{\omega}X$, $\eta_2 = 2\omega T - \sqrt{2\omega}X$, $\eta_3 = (1+\omega)T - \sqrt{1+\omega}X$, $\eta_4 = (1-\omega)T - \sqrt{1-\omega}X$.